Computers and Fluids 244 (2022) 105584

Contents lists available at ScienceDirect

Computers and Fluids

journal homepage: www.elsevier.com/locate/compfluid

A simplified multilayer perceptron detector for the hybrid WENO scheme

Zhengyang Xue [a,b], Yinhua Xia [a,*], Chen Li [b,*], Xianxu Yuan [b]

[a] School of Mathematical Sciences, University of Science and Technology of China, Hefei, Anhui 230026, PR China
[b] State Key Laboratory of Aerodynamics, Mianyang, Sichuan 621000, PR China

ARTICLE INFO

Keywords:
Hybrid WENO scheme
Multilayer perceptron
Smoothness detector
Euler equations

ABSTRACT

This paper develops a Multilayer Perceptron (MLP) smoothness detector for the hybrid WENO scheme. Since the MLP detector contains nonlinear activation functions and large matrix operators, we analyze and reduce it to a simplified MLP (SMLP) detector for efficiency. In the hybrid WENO scheme, both detectors can be adopted to identify whether the reconstruction stencil is a smooth region or not. To improve the spectral resolution of the hybrid scheme, a high-frequency region is introduced. Thus, the high order linear reconstruction, WENO type reconstruction, and blending reconstruction are performed on the smooth, non-smooth, and high-frequency regions. Numerical tests and comparisons for Euler equations are presented to demonstrate the robustness and performance of the hybrid scheme and the efficiency of the simplified MLP detector.

1. Introduction

High-fidelity numerical methods are widely used in fluid dynamics nowadays [1,2], such as the discontinuous Galerkin methods [3–5] and the weighted essentially non-oscillatory (WENO) schemes [6,7]. In particular, the WENO scheme can provide numerical solutions with high order accuracy in the smooth region and essentially non-oscillatory (ENO) property near discontinuity, which makes it a popular choice for simulating supersonic or hypersonic flows.

However, the original WENO scheme has at least two drawbacks, i.e., order-degradation near the critical points and over-dissipation for the scale-resolved simulations. To overcome the former defect, a specific uniform function [8] was used to map the original nonlinear weights to the new ones. Besides, Borges et al. [9] introduced a global smoothness indicator to reformulate the nonlinear weighting procedure, named WENOZ. To cover the latter deficiency, adding a downwind candidate stencil, which results in a central-type scheme, is a common strategy to enhance the spectral resolution of the scheme. Martín et al. [10] and Sun et al. [11] devised central-type schemes with bandwidth optimization and minimizing the dissipation for direct numerical simulation of compressible turbulence. Hu et al. [12], and Li et al. [13] proposed the central-type WENO schemes by improving the global smoothness indicators, which results in good enhancements in the turbulent simulations. Additionally, a symmetric sixth-order targeted ENO scheme [14] with the idea of excluding the less smooth sub-stencils, was applied to the turbulent channel flow [15].

Besides, the hybrid WENO scheme is an alternative remedy for the shortcomings of the original WENO scheme. One of the key elements of the hybrid WENO scheme is the discontinuity indicator, which greatly influences the performance of the corresponding hybrid scheme. Taking the compact-WENO scheme [16] as an example, a low threshold of the density-based indicator yields over-dissipative for smooth regions, whereas a high value may affect the robustness of shock-capturing. Apart from the feature-based discontinuity indicators [17,18], many indicators are in cooperation with the WENO schemes. Zhao et al. [19] devised a discontinuity indicator based on the divergence between the nonlinear weights and ideal weights. Hill et al. [20], Liu et al. [21] and Li et al. [13] proposed the indicators based on different functions of smoothness measurements, respectively. Moreover, comparisons of the performances of the hybrid WENO schemes were presented [22] using nine limiter-based indicators from discontinuous Galerkin (DG) methods. The numerical tests in Refs. [13,17–21] demonstrated that the hybrid scheme is a practical strategy to get a balance between high accuracy for multi-scale flow structures and robustness for shock capturing. However, the parameters or the thresholds in most of the indicators above are full of empiricism, even artificially set case-by-case.

Machine learning (ML) is an emerging tool to tackle this issue, and it has made significant developments in fluid mechanics [23] recently. In particular, some progress was made by incorporating ML-based shock detection techniques into the high-fidelity numerical methods. Wen et al. [24] proposed an artificial neural network (ANN) edge detector and developed a hybrid fifth-order Compact-WENO finite difference scheme. Sun et al. [25] trained a convolution neural network (CNN)-based discontinuity indicator and combined the WENO scheme

* Corresponding authors.
E-mail addresses: zhyxue@mail.ustc.edu.cn (Z. Xue), yhxia@ustc.edu.cn (Y. Xia), lichen@skla.cardc.cn (C. Li), yuanxianxu@cardc.cn (X. Yuan).

https://doi.org/10.1016/j.compfluid.2022.105584
Received 6 December 2021; Received in revised form 3 May 2022; Accepted 28 June 2022
Available online 30 June 2022
0045-7930/© 2022 Elsevier Ltd. All rights reserved.

with a six-order central difference scheme. Besides, more ML-based indicators are proposed in the DG method for solving nonlinear hyperbolic conservation laws. Feng et al. [26] presented a characteristic-featured indicator on the structured mesh by training an artificial neuron without activation function in the hidden layer and extended it to unstructured mesh later [27]. Ray and Hesthaven [28] proposed an indicator by training a specific type of ANN, known as a multilayer perceptron (MLP), with five hidden layers, and a minor architecture was further adopted in Ref. [29] for unstructured meshes in two dimensions. To enhance the performance of the limiter-based indicator, Yu and Shu [30] developed a TVB constant MLP-based estimator with automatically selecting M in the TVB limiter, other than the classical choice through trial and error. Another troubled-cell indicator was proposed [31] using K-means clustering with the KXRCF indication variable and obtained better performance compared with the original KXRCF limiter. Apart from using the limiters to control spurious oscillations near the discontinuities, Discacciati et al. [32] developed the artificial viscosity method with an MLP-based indicator, which also outperforms the classical artificial viscosity models. The ML-indicators' advantage over traditional counterparts is that they do not contain any problem-independent parameters. In contrast, most of them are used as black boxes, and the neural networks are of high complexity and lack interpretability.

Inspired by the above works, we aim to construct a simple MLP-based "smoothness" detector for the hybrid WENO scheme. The network is trained offline using a supervised learning strategy. And we analyze and simplify the MLP detector for efficiency. Then, both the MLP detector and the simplified one are adopted in the hybrid scheme by separating the troubled stencil from the numerical solution. In the hybrid strategy [33], the troubled stencil is further labeled as a high-frequency or non-smooth stencil to enhance the performance of the hybrid scheme. Thus, the high-order linear, WENO-type, and blending reconstructions are performed on the smooth, non-smooth, and high-frequency regions, respectively. The new hybrid WENO schemes have high resolution and robustness for various flows with shock waves.

The remainder of this paper is organized as follows. In Section 2, we briefly review the finite difference WENO scheme and the framework of the hybrid WENO scheme. The algorithm of the MLP-based smoothness detector and the expression of the simplified MLP (SMLP) detector are described in Section 3. Numerical examples for Euler equations with shock waves are provided in Section 4 to demonstrate the capability of the efficiency of the detectors and the high fidelity of the new hybrid scheme. Conclusions are given in Section 5.

2. Finite difference WENO method for hyperbolic conservation laws

This section will briefly review the finite difference WENO method for hyperbolic conservation laws and the hybrid approach. We will mainly focus on the most popular fifth-order scheme to illustrate the procedure.

2.1. Finite difference WENO method for conservation laws

Consider the following scalar conservation law:

$$\begin{cases} u_t + f(u)_x = 0, \quad x \in [a,b], \\ u(x,0) = u_0(x), \end{cases} \tag{2.1}$$

with the periodic boundary condition for simplicity. On a uniform grid $a = x_{\frac{1}{2}} < x_{\frac{3}{2}} < \cdots < x_{N+\frac{1}{2}} = b$, define mesh size $\Delta x = x_{j+\frac{1}{2}} - x_{j-\frac{1}{2}}$, a semidiscrete conservative high-order finite difference scheme of (2.1) is

$$\frac{d}{dt}u_j + \frac{1}{\Delta x}\left(\hat{f}_{j+\frac{1}{2}} - \hat{f}_{j-\frac{1}{2}}\right) = 0, \tag{2.2}$$

where u_j is an approximation to the point value $u(x_j, t)$, and the numerical flux $\hat{f}_{j+\frac{1}{2}} = \hat{f}\left(u_{j-r}, \dots, u_{j+s}\right)$ is designed to approximate the sliding function $h(x_{j+\frac{1}{2}})$ to a high-order accuracy which is defined by

$$\frac{1}{\Delta x}\int_{x-\frac{\Delta x}{2}}^{x+\frac{\Delta x}{2}} h(\xi)d\xi = f(u(x)). \tag{2.3}$$

In order to ensure stability, the flux splitting approach is used to divide the flux into positive and negative parts $\hat{f}_{j+\frac{1}{2}} = \hat{f}^+_{j+\frac{1}{2}} + \hat{f}^-_{j+\frac{1}{2}}$, e.g. the Lax–Friedrichs flux splitting as follows

$$f^{\pm}(u) = \frac{1}{2}(f(u) \pm \alpha u), \quad \alpha = \max_u \left|f'(u)\right|. \tag{2.4}$$

The basic idea of the WENO method is to use the smoothness indicators to automatically select the weight of sub-stencils and then sum them to avoid oscillation. In the fifth-order WENOJS method [7], the numerical flux $\hat{f}^+_{j+\frac{1}{2}}$ is reconstructed by

$$\hat{f}^+_{j+\frac{1}{2}} = \omega_0 q_0 + \omega_1 q_1 + \omega_2 q_2, \tag{2.5}$$

where q_k is the value at $x_{j+\frac{1}{2}}$ obtained by low-order reconstruction on each sub-stencil,

$$q_0 = \frac{1}{3}f^+_{j-2} - \frac{7}{6}f^+_{j-1} + \frac{11}{6}f^+_j, \tag{2.6}$$

$$q_1 = -\frac{1}{6}f^+_{j-1} + \frac{5}{6}f^+_j + \frac{1}{3}f^+_{j+1}, \tag{2.7}$$

$$q_2 = \frac{1}{3}f^+_j + \frac{7}{6}f^+_{j+1} - \frac{1}{6}f^+_{j+2}. \tag{2.8}$$

And the nonlinear weights ω_k are obtained by

$$\omega_k = \frac{\alpha_k}{\sum_{l=0}^2 \alpha_l}, \quad \text{with} \quad \alpha_k = \frac{d_k}{(\varepsilon + \beta_k)^2}, \quad k = 0,1,2, \tag{2.9}$$

with the smoothness indicators β_k defined by

$$\beta_0 = \frac{13}{12}\left(f^+_{j-2} - 2f^+_{j-1} + f^+_j\right)^2 + \frac{1}{4}\left(f^+_{j-2} - 4f^+_{j-1} + 3f^+_j\right)^2, \tag{2.10}$$

$$\beta_1 = \frac{13}{12}\left(f^+_{j-1} - 2f^+_j + f^+_{j+1}\right)^2 + \frac{1}{4}\left(f^+_{j-1} - f^+_{j+1}\right)^2, \tag{2.11}$$

$$\beta_2 = \frac{13}{12}\left(f^+_j - 2f^+_{j+1} + f^+_{j+2}\right)^2 + \frac{1}{4}\left(3f^+_j - 4f^+_{j+1} + f^+_{j+2}\right)^2, \tag{2.12}$$

and the linear weights, $d_0 = \frac{3}{10}$, $d_1 = \frac{3}{5}$ and $d_2 = \frac{1}{10}$. The parameter ε is taken as 10^{-6} for example to avoid the denominator being 0. The reconstruction of $f^-_{j+\frac{1}{2}}$ is a mirror symmetry to that $f^+_{j+\frac{1}{2}}$ with respect to $x_{j+\frac{1}{2}}$.

Another popular method is the WENOZ reconstruction [9], which adopt a global smoothness indicator $\tau = |\beta_0 - \beta_2|$, and the new nonlinear weights are as follows

$$\omega^z_k = \frac{\alpha^z_k}{\sum_{l=0}^2 \alpha^z_l}, \quad \text{with } \alpha^z_k = d_k\left(1 + \frac{\tau}{\beta_k + \varepsilon}\right), \quad \varepsilon = 10^{-40}, \quad k = 0,1,2. \tag{2.13}$$

For the one-dimensional hyperbolic system

$$\begin{cases} \boldsymbol{u}_t + \boldsymbol{F}(\boldsymbol{u})_x = \boldsymbol{0}, \quad x \in [a,b], \\ \boldsymbol{u}(x,0) = \boldsymbol{u}_0(x), \end{cases} \tag{2.14}$$

usually the characteristic decomposition is used rather than the component-wise reconstruction in order to make the algorithm more robust. First, the Roe average [34] is performed to obtain the right eigenvector $\boldsymbol{R}_{j+\frac{1}{2}}$, the left eigenvector $\boldsymbol{R}^{-1}_{j+\frac{1}{2}}$ and the eigenvalues $\boldsymbol{\Lambda}_{j+\frac{1}{2}}$ of the Jacobian $\boldsymbol{F}'(u_{j+\frac{1}{2}})$. Transform the conservative variables $\boldsymbol{U}_{i+\frac{1}{2}}$ and fluxes $\boldsymbol{F}_{i+\frac{1}{2}}$ to the characteristic variables $\boldsymbol{V}_{i+\frac{1}{2}}$ and fluxes $\boldsymbol{G}_{i+\frac{1}{2}}$ by $\boldsymbol{V}_{i+\frac{1}{2}} = \boldsymbol{R}^{-1}_{j+\frac{1}{2}}\boldsymbol{U}_{i+\frac{1}{2}}$ and $\boldsymbol{G}_{i+\frac{1}{2}} = \boldsymbol{R}^{-1}_{j+\frac{1}{2}}\boldsymbol{F}_{i+\frac{1}{2}}$ for i in a neighborhood of j. Second, adopt WENO reconstruction for each component of the characteristic variables to obtain $\boldsymbol{G}^{\pm}_{j+\frac{1}{2}}$. Then, transform them back into physical space by using $\boldsymbol{F}^{\pm}_{j+\frac{1}{2}} = \boldsymbol{R}_{j+\frac{1}{2}}\boldsymbol{G}^{\pm}_{j+\frac{1}{2}}$ and obtain the numerical fluxes $\boldsymbol{F}_{j+\frac{1}{2}} = \boldsymbol{F}^{+}_{j+\frac{1}{2}} + \boldsymbol{F}^{-}_{j+\frac{1}{2}}$.

For multi-dimensional problems, the WENO reconstruction can be done in a dimension by dimension fashion. After the space is discretized, the semi-discrete system $u_t = L(u,t)$ can be solved by the popular strong-stability preserving Runge–Kutta (SSP-RK) method [35], e.g. the third-order one with given u^n to obtain u^{n+1} by:

$$\begin{cases} u^{(1)} &= u^n + \Delta t L\left(u^n, t^n\right), \\ u^{(2)} &= \frac{3}{4}u^n + \frac{1}{4}u^{(1)} + \frac{1}{4}\Delta t L\left(u^{(1)}, t^n + \Delta t\right), \\ u^{n+1} &= \frac{1}{3}u^n + \frac{2}{3}u^{(2)} + \frac{2}{3}\Delta t L\left(u^{(2)}, t^n + \frac{1}{2}\Delta t\right), \end{cases} \tag{2.15}$$

where Δt is a suitable time step. We refer to [36] for more details of WENO methods for conservation laws.

2.2. Hybrid scheme for conservation laws

For the hybrid scheme, we adopt the approach in [33], which identifies the stencil into three categories, the smooth stencil, the non-smooth stencil, and the high-frequency stencil, to achieve better spectral performance for problems with delicate structures. The fifth-order linear upwind reconstruction is adopted in the smooth stencil for the fifth-order scheme. In the non-smooth stencil, a specific WENO reconstruction is used to achieve the ENO property of the scheme. If all sub-stencils are not smooth enough, the stencil is marked as a high-frequency one, and a blending WENO reconstruction is performed.

By some specific smoothness detector, e.g., the MLP detector to be developed in the following section, we first determine whether the stencil is smooth. If it is not smooth enough, then the stencil is distinguished as a high-frequency or non-smooth one as follows. Calculate the minimum value β_A of the three smoothness metrics β_0, β_1 and β_2. If all sub-stencils contain discontinuities, it can be measured by $\beta_A > C\Delta x$, which means it is a high-frequency region. Otherwise, the stencil contains at least one smooth sub-stencil and is marked as the non-smooth region.

In the high-frequency stencil, the fifth-order blending WENO reconstruction is performed as follows. First, we calculate the smoothness indicator β_L for the fifth-order linear reconstruction $P^4(x)$ as the smoothness indicators β_i, $i = 0, 1, 2$ for three sub-stencils

$$\beta_L = \sum_{r=1}^{4} h^{2r-1} \int_{x_{i-\frac{1}{2}}}^{x_{i+\frac{1}{2}}} \left(\left(P^4(x)\right)^{(r)}\right)^2 \,\mathrm{d}x. \tag{2.16}$$

The blending reconstruction is the convex combination of the linear reconstruction and the WENO reconstruction with the weights ω_L and $1-\omega_L$ respectively. The ω_L is obtained by

$$\omega_L = \min\left(1, \frac{1+\sqrt{1+(a+1)(Q-1)}}{a+1}\right), \tag{2.17}$$

where $a = \frac{\beta_L}{\beta_A}$, and Q is the amplification factor.

3. The multilayer perceptron smoothness detector

This section will introduce the multilayer perceptron (MLP) smoothness detector to identify whether the reconstruction stencil is smooth.

3.1. Error metrics and the multilayer perceptron architecture

In the fifth-order finite difference WENO scheme, there are five points $\{f_i\}_{i=j-2,\ldots,j+2}$ for each reconstruction. Wen et al. [24] used the five points as input to train the artificial neural network. Besides, to judge a discontinuity should also be related to the mesh size Δx. We calculate the three error metrics as feature reduction, so the inputs are reduced from six to four metrics. Taking three-point sub-stencils

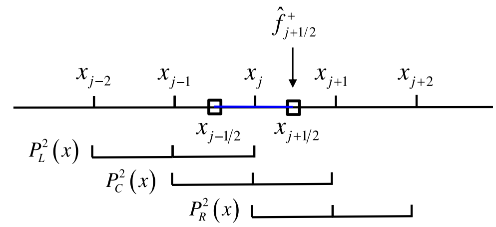

Fig. 3.1. The three-point sub-stencils for constructing P_L^2, P_C^2 and P_R^2.

from left to right in turn, we obtain three second degree polynomials, denoted as P_L^2, P_C^2 and P_R^2, as shown in Fig. 3.1. Then calculate the L_2 error of the two polynomials in $[x_{j-\frac{1}{2}}, x_{j+\frac{1}{2}}]$, which gives the following error metrics E_{LC}, E_{CR}, E_{LR},

$$E_{LC} = \frac{1}{\Delta x}\left\|P_L^2(x) - P_C^2(x)\right\|_{L_2}^2 = \frac{23}{960}\left(f_{j-2} - 3f_{j-1} + 3f_j - f_{j+1}\right)^2, \tag{3.1}$$

$$E_{CR} = \frac{1}{\Delta x}\left\|P_C^2(x) - P_R^2(x)\right\|_{L_2}^2 = \frac{23}{960}(f_{j-1} - 3f_j + 3f_{j+1} - f_{j+2})^2, \tag{3.2}$$

$$\begin{aligned} E_{LR} = \frac{1}{\Delta x}\left\|P_L^2(x) - P_R^2(x)\right\|_{L_2}^2 &= \frac{1}{320}\left(-f_{j-2} + 2f_{j-1} - 2f_{j+1} + f_{j+2}\right)^2 \\ &\quad + \frac{1}{48}\left(f_{j-2} - 4f_{j-1} + 6f_j - 4f_{j+1} + f_{j+2}\right)^2. \end{aligned} \tag{3.3}$$

The expansions of formula (3.1) to (3.3) in Taylor series at x_j are

$$E_{LC} = \frac{23}{960}\left(f_j^{(3)}\right)^2 \Delta x^6 + \mathcal{O}(\Delta x^7), \tag{3.4}$$

$$E_{CR} = \frac{23}{960}\left(f_j^{(3)}\right)^2 \Delta x^6 + \mathcal{O}(\Delta x^7), \tag{3.5}$$

$$E_{LR} = \frac{1}{80}\left(f_j^{(3)}\right)^2 \Delta x^6 + \mathcal{O}(\Delta x^7), \tag{3.6}$$

when the function $f(x)$ is sufficiently smooth.

Here we introduce the MLP architecture as in Fig. 3.2, a fully connected neural network with four inputs, one hidden layer and two outputs. Based on a prior information, we choose three error metrics E_{LC}, E_{CR}, E_{CR} and mesh size Δx as inputs to judge whether the stencil is good. The hidden layer contains 256 neurons, and rectified linear unit $\mathrm{ReLU}(x) = \max(x, 0)$ is chosen as the activation function to achieve nonlinearity. In the outputs layer, softmax function $\mathrm{Softmax}(x) = \frac{e^{x_i}}{\sum_{j=1}^{n} e^{x_j}}$ is chosen as the activation function to obtain the probability of smooth stencil $\hat{y}_0$ and troubled stencil $\hat{y}_1$. We use label to represent the classification result, and

$$\begin{cases} \hat{y}_0 > \hat{y}_1 \Rightarrow \text{label} = 0, & \text{smooth stencil}, \\ \hat{y}_0 < \hat{y}_1 \Rightarrow \text{label} = 1, & \text{troubled-stencil}. \end{cases} \tag{3.7}$$

3.2. Construction of the training sets and validation sets

Inspired by the work of Sun et al. [25], the numerical solution is a little different from the exact solution because of numerical dissipation or spurious oscillation, especially near the discontinuities. Two different strategies are used to generate the data sets. One is related to the numerical methods, and the other is the artificially constructed function class. For simplicity of presentation, we denote by $a \sim U(D)$ if a is a random variable with a uniform distribution on D.

First, we generate the data for the training sets $\mathbb{T}$ of troubled stencils. Consider the following one-dimensional linear advection equation

$$\begin{cases} u_t + a u_x = 0, x \in [-1, 1], \\ u(x, 0) = \begin{cases} 0, & x < 0, \\ u_R, & x > 0. \end{cases} \end{cases} \tag{3.8}$$

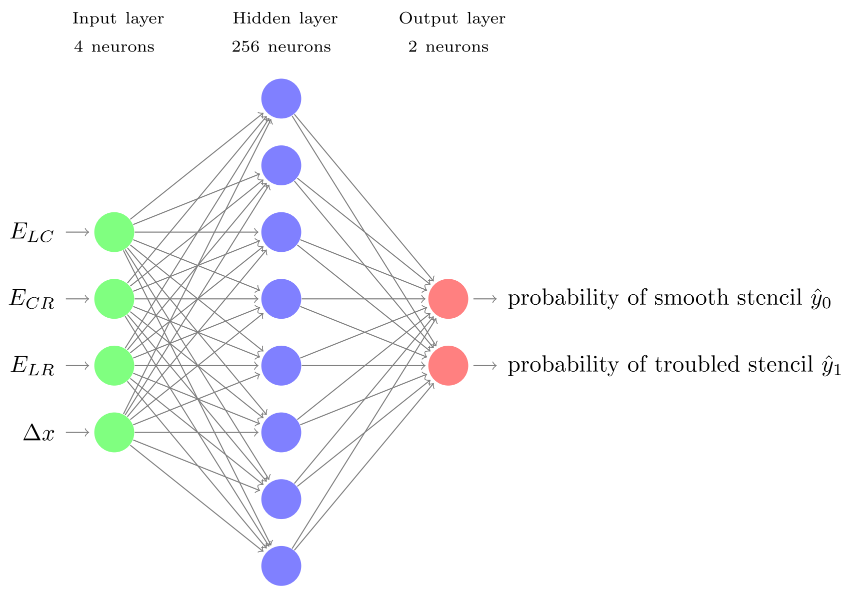

Fig. 3.2. The MLP architecture.

where the advection coefficient $a \sim U(\{-1,1\})$, and the initial jump $u_R \in [-1,1]$. It is easy to obtain the exact solution is $u(x,T) = u(x-aT)$ and the discontinuity is located at $x_0 = aT$ at time $t = T$. Here the time is chosen as $T = N_t \frac{\Delta x}{6}$, where the number of time step $N_t \sim U(\{1,2,3,4\})$ and the mesh sizes $\Delta x \in [0.001, 0.1]$. Three sets of solutions are obtained by the following methods:

(1) the fifth-order linear upwind finite difference method with the third-order SSP-RK method,
(2) the fifth-order finite difference WENOJS method with the third-order SSP-RK method,
(3) the exact solution formula.

We only retain the stencils that contain discontinuities in each set of solutions.

Next, we generate the data for the training sets $\mathbb{T}$ of smooth stencil. The smooth stencil data consists of random polynomial series

$$P^k(x) = \sum_{n=0}^{k} a_n x^n, \quad x \in [-2,2], \tag{3.9}$$

where $k \sim U(\{2,3,4,5\})$ and a_n are independent and identically distributed random variables. The mesh sizes Δx are the same as that used to generate the data of troubled stencils. Here the error metrics are used as input, so that the results of the $P^k, k \le 2$ polynomial series are all zero. In order to maintain the unbiasedness of data labels, the training set include 10,000 data from troubled stencils and 10,000 data from smooth stencils.

For the validation sets $\mathbb{V}$, a part of it should be different from the training sets $\mathbb{T}$, which comes from solving the Burgers equation in order to measure the generalization of the training model. Consider the following Burgers equation with periodic boundary condition

$$\begin{cases} u_t + \left(\frac{u^2}{2}\right)_x = 0, & x \in [-\pi, \pi], \\ u(x,0) = 0.5 + \sin(x). \end{cases} \tag{3.10}$$

We can use the characteristic method and Newton iteration to get the exact solution and the shock wave location. The data includes numerical solutions and exact solutions. The validation set $\mathbb{V}$ includes 3000 data generated in the same way as the training sets $\mathbb{V}$ and 5000 data from the Burgers equation.

3.3. Training the MLP model

Before calculating the error metrics for each sample $\left(f_{j-2}, f_{j-1}, f_j, f_{j+1}, f_{j+2}\right)$, we first use data preprocessing technology by

$$\hat{f}_i = \frac{f_i}{\max_{k=j-2,\dots,j+2}\left(|f_k|, 1\right)}, \quad i = j-2, \dots, j+2. \tag{3.11}$$

This step eliminates the influence of the function value, so that the data are all in $[0,1]$. Finally, cross entropy loss function [37] are used to measure the error result of classification, which is

$$\mathcal{L} = -\frac{1}{M}\sum_{k=1}^{M} y_0^k \log\left(\hat{y}_0^k\right) + \left(1-y_0^k\right)\log\left(1-\hat{y}_0^k\right), \tag{3.12}$$

where M is the number of samples, $\hat{y}_0^k$ and y_0^k represent the predicted and true smooth probabilities of the stencil for the kth sample respectively. The weight parameters in MLP are initialized based on a normal distribution. The entire model is built by PyTorch. The optimizer is Adam optimization [38] with batch size of 256, and learning rate equals 0.001 with 5000 iterations. Finally, we choose the training model that have an accuracy rate of more than 95% on both the validation sets $\mathbb{V}$ and the training sets $\mathbb{T}$.

3.4. Simplified MLP troubled-stencil indicator

The MLP is composed of complex nonlinear activation functions and many matrix operations to achieve good approximation capabilities. But it is a black box and relatively expensive. So we want to simplify the MLP detector by checking the outputs carefully.

We denote the set of parameters $\boldsymbol{\theta}$ in the MLP detector by

$$\boldsymbol{\theta} = \left(\boldsymbol{W}^{[0]} \in \mathbb{R}^{256\times4}, \boldsymbol{W}^{[1]} \in \mathbb{R}^{2\times256}, \boldsymbol{b}^{[0]} \in \mathbb{R}^{256}.\boldsymbol{b}^{[1]} \in \mathbb{R}^{2}\right), \tag{3.13}$$

where $\boldsymbol{W}^{[0]}$ and $\boldsymbol{W}^{[1]}$ are the weights of the input layer and the hidden layer respectively, and $\boldsymbol{b}^{[0]}$ and $\boldsymbol{b}^{[1]}$ are the biases of the input layer and the hidden layer respectively. The input is denoted as $\boldsymbol{x}^{[0]} = \left(E_{LC}, E_{CR}, E_{LR}, \Delta x\right)^T$, and the output is denoted as $\boldsymbol{y} = \left(\hat{y}_0, \hat{y}_1\right)^T$. The MLP detector can be written as the following composite functions

$$\boldsymbol{x}^{[1]} = \mathrm{ReLU}\left(\boldsymbol{W}^{[0]}\boldsymbol{x}^{[0]} + \boldsymbol{b}^{[0]}\right), \tag{3.14}$$

$$\boldsymbol{x}^{[2]} = \boldsymbol{W}^{[1]}\boldsymbol{x}^{[1]} + \boldsymbol{b}^{[1]}, \tag{3.15}$$

$$\boldsymbol{y} = \mathrm{softmax}\left(\boldsymbol{x}^{[2]}\right), \tag{3.16}$$

denoted by

$$\boldsymbol{y} = \boldsymbol{\mathcal{H}}_{MLP}(\boldsymbol{x}^{[0]}). \tag{3.17}$$

Assume the input data is sufficiently smooth, the input $\boldsymbol{x}^{[0]} \sim \left(\mathcal{O}(\Delta x^6), \mathcal{O}(\Delta x^6), \mathcal{O}(\Delta x^6), \Delta x\right)^T$. We can obtain the following linear approximation

$$\boldsymbol{x}^{[1]} = \mathrm{ReLU}\left(\boldsymbol{W}^{[0]}\boldsymbol{x}^{[0]} + \boldsymbol{b}^{[0]}\right) \approx \boldsymbol{W}^{[0]}_{\mathrm{mod}}\boldsymbol{x}^{[0]} + \boldsymbol{b}^{[0]}_{\mathrm{mod}}, \tag{3.18}$$

where $\boldsymbol{W}^{[0]}_{\mathrm{mod}} \in \mathbb{R}^{256\times 4}$, $\boldsymbol{b}^{[0]}_{\mathrm{mod}} \in \mathbb{R}^{256}$. Taking formula (3.18) into formula (3.15), then we get

$$\begin{aligned}\boldsymbol{x}^{[2]} &\approx \boldsymbol{W}^{[1]}\left(\boldsymbol{W}^{[0]}_{\mathrm{mod}}\boldsymbol{x}^{[0]} + \boldsymbol{b}^{[0]}_{\mathrm{mod}}\right) + \boldsymbol{b}^{[1]} \\ &= \boldsymbol{W}\boldsymbol{x}^{[0]} + \boldsymbol{b}.\end{aligned} \tag{3.19}$$

where $\boldsymbol{W} = \boldsymbol{W}^{[1]}\boldsymbol{W}^{[0]}_{\mathrm{mod}}$ and $\boldsymbol{b} = \boldsymbol{W}^{[1]}\boldsymbol{b}^{[0]}_{\mathrm{mod}} + \boldsymbol{b}^{[1]}$.

The softmax function in the output layer is just for normalization, and $\hat{y}_0 > \hat{y}_1$ is equivalents to $\boldsymbol{x}^{[2]}_1 > \boldsymbol{x}^{[2]}_2$. Then we can use the value of $\boldsymbol{x}^{[2]}_1 - \boldsymbol{x}^{[2]}_2$ to judge the label. According to the approximation (3.19), we have

$$\begin{aligned}\boldsymbol{x}^{[2]}_1 - \boldsymbol{x}^{[2]}_2 &= \sum_{j=1}^{4}\left(\boldsymbol{W}_{1,j} - \boldsymbol{W}_{2,j}\right)\boldsymbol{x}^{[0]}_j + \left(\boldsymbol{b}_1 - \boldsymbol{b}_2\right) \\ &= \left|\boldsymbol{b}_1 - \boldsymbol{b}_2\right|\left(\sum_{j=1}^{4}\frac{\boldsymbol{W}_{1,j} - \boldsymbol{W}_{2,j}}{\left|\boldsymbol{b}_1 - \boldsymbol{b}_2\right|}\boldsymbol{x}^{[0]}_j + \mathrm{sgn}\left(\boldsymbol{b}_1 - \boldsymbol{b}_2\right)\right).\end{aligned} \tag{3.20}$$

Thus the simplified MLP detector function can be defined as follows

$$\mathcal{H}_{SMLP}\left(E_{LC}, E_{CR}, E_{LR}, \Delta x\right) = w_{LC}E_{LC} + w_{CR}E_{CR} + w_{LR}E_{LR} + w_h\Delta x + b, \tag{3.21}$$

where $w_{LC} = \frac{\boldsymbol{W}_{1,1}-\boldsymbol{W}_{2,1}}{|\boldsymbol{b}_1-\boldsymbol{b}_2|}, w_{CR} = \frac{\boldsymbol{W}_{1,2}-\boldsymbol{W}_{2,2}}{|\boldsymbol{b}_1-\boldsymbol{b}_2|}, w_{LR} = \frac{\boldsymbol{W}_{1,3}-\boldsymbol{W}_{2,3}}{|\boldsymbol{b}_1-\boldsymbol{b}_2|}, w_h = \frac{\boldsymbol{W}_{1,4}-\boldsymbol{W}_{2,4}}{|\boldsymbol{b}_1-\boldsymbol{b}_2|}$ and $b = \mathrm{sgn}\left(\boldsymbol{b}_1 - \boldsymbol{b}_2\right)$. For $\mathcal{H}_{SMLP}\left(E_{LC}, E_{CR}, E_{LR}, \Delta x\right) > 0$ the stencil is "smooth", otherwise it is a trouble one.

The interesting result is that the distribution of coefficients is neat as shown in Fig. 3.3. Note that $\mathcal{H}_{SMLP}\left(E_{LC}, E_{CR}, E_{LR}, \Delta x\right)$ is a piecewise linear function, and the coefficients are given by

$$\begin{aligned}&\left(w_{LC}, w_{CR}, w_{LR}, w_h, b\right) \\ &= \begin{cases}(-71902.289, -73288.375, -87095.492, 32.400, 1), & \Delta x \in (0, 0.0011], \\ (-71062.297, -72432.172, -86096.359, 22.939, 1), & \Delta x \in (0.0011, 0.0014], \\ (-70222.313, -71575.977, -85097.219, 13.477, 1), & \Delta x \in (0.0014, 0.018], \\ (-70515.172, -71874.508, -85451.891, 13.763, 1), & \Delta x \in (0.018, 0.05], \\ (-23766.861, -24225.002, -28797.424, -8.640, 1), & \Delta x \in (0.05, 0.076], \\ (-27398.197, -27927.742, -33171.141, -7.972, 1), & \Delta x \in (0.076, 0.078], \\ (-33540.254, -34190.500, -40570.602, -6.888, 1), & \Delta x \in (0.078, 0.1].\end{cases}\end{aligned} \tag{3.22}$$

Comparing the MLP detector $\mathcal{H}_{MLP}$ in (3.14)–(3.17) and the simplified one $\mathcal{H}_{SMLP}$ in (3.21)–(3.22), the MLP detector function contains the multiplication of matrix and vector of about 256 × 13 operations. The simplified one contains only 8 operations. In the following numerical tests, we will compare the efficiency and performance of these two detectors. Finally, we summarize our MLP/SMLP hybrid reconstruction procedure in the Algorithm 3.1.

In the following numerical tests, we take the parameter $C = 1$ and $Q = 9$ as in [33] and the WENOJS and WENOZ schemes for hybridizing. The dispersion and dissipation properties of the fifth-order hybrid schemes are discussed here by the approximate dispersion relation [39]. It is observed from Fig. 3.4 that the hybrid schemes all improve the spectral properties of the original WENOJS and WENOZ methods. And the spectral properties of hybrid schemes WENOJS/WENOZ-H-MLP and WENOJS/WENOZ-H-SMLP are highly similar.

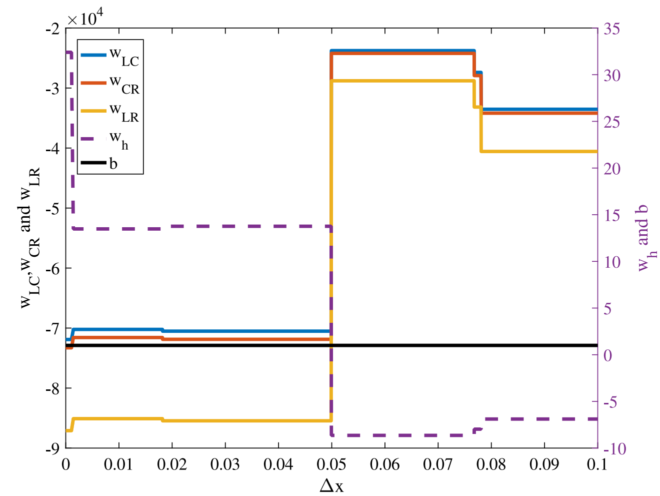

Fig. 3.3. Coefficients of the simplified MLP detector function $\mathcal{H}_{SMLP}\left(E_{LC}, E_{CR}, E_{LR}, \Delta x\right)$.

Algorithm 3.1 WENO-H-MLP/SMLP

Input: $\left(f_{j-2}, f_{j-1}, f_j, f_{j+1}, f_{j+2}\right)$ and mesh size Δx for reconstruction.
Output: Reconstruct the value of f .
1: Preprocessing: Calculate error metrics E_{LC}, E_{CR}, E_{LR} after the scaling $\hat{f}_i = \frac{f_i}{\max_{k=j-2,\ldots,j+2}(|f_k|,1)}, \quad i = j-2, \ldots, j+2.$
2: **if** $\boldsymbol{\mathcal{H}}_{MLP}/\mathcal{H}_{SMLP}\left(E_{LC}, E_{CR}, E_{LR}, \Delta x\right)$ judges that the stencil is smooth, **then**
3: Perform the high order linear reconstruction.
4: **else if** $\beta_A > C\Delta x$ **then**
5: Perform the blending reconstruction.
6: **else**
7: Perform the specific WENO reconstruction.
8: **end if**

4. Numerical tests

This section performs numerical tests by using the fifth-order WENOJS/WENOZ-H-MLP and WENOJS/WENOZ-H-SMLP schemes for Euler equations. The two-dimensional Euler equations is given by

$$\begin{pmatrix}\rho\\ \rho u\\ \rho v\\ E\end{pmatrix}_t + \begin{pmatrix}\rho u\\ \rho u^2 + p\\ \rho uv\\ u(E+p)\end{pmatrix}_x + \begin{pmatrix}\rho v\\ \rho uv\\ \rho v^2 + p\\ v(E+p)\end{pmatrix}_y = \boldsymbol{0}. \tag{4.1}$$

Here ρ is the density, (u, v) is the velocity, and E is the total internal energy. The pressure p satisfies the ideal gas equation of state, $p = (\gamma-1)\left(E - \frac{1}{2}\rho u^2\right)$ in the one dimension and $p = (\gamma-1)\left(E - \frac{1}{2}\rho(u^2 + v^2)\right)$ in the two dimensions. γ is the ratio of specific heats, and $\gamma = 1.4$ for air.

For each test, the percentage of non-smooth stencil Ns and high-frequency stencil Hf are counted in the entire calculation process. The sum of Ns and Hf is recorded as Ts, the percentage of troubled stencils marked by the MLP or SMLP detectors. The ratio of Ts on the coarse grid and the double refined grid is introduced to inspect the robustness of the indicator, denoted as RI, which should be close to 0.5 in the ideal scenario. The CPU time cost ratio of the WENO-H-MLP scheme to the WENO-H-SMLP scheme, denoted by RT, is also recorded to compare the efficiency of the two detectors. These numerical tests can also be found partially in some recent papers on high order WENO schemes [40–43], which can be used for numerical performance comparison.

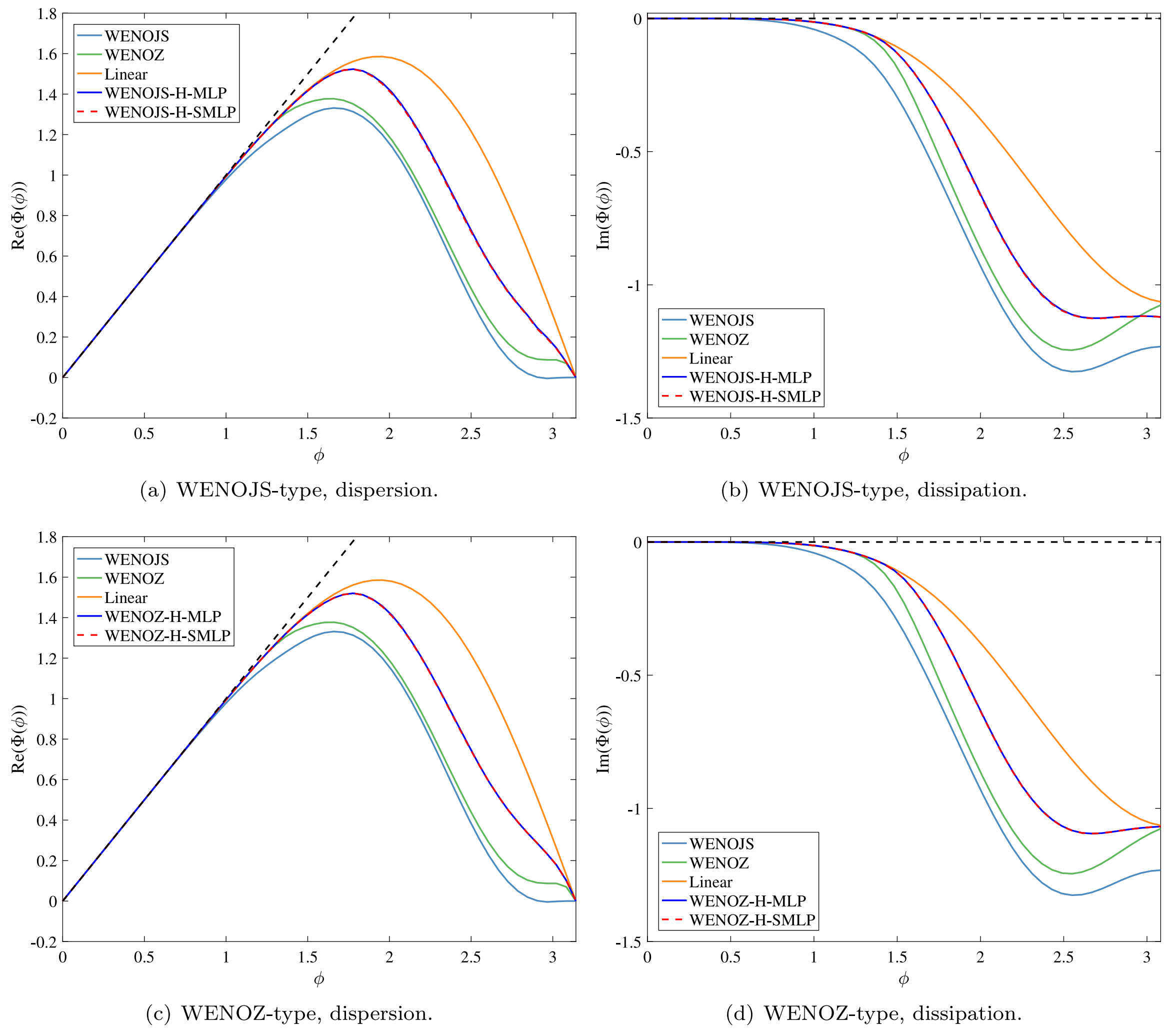

(a) WENOJS-type, dispersion.
(b) WENOJS-type, dissipation.
(c) WENOZ-type, dispersion.
(d) WENOZ-type, dissipation.

Fig. 3.4. Approximate dispersion and dissipation relations for different schemes.

Example 4.1 (*The Lax Problem*). The Lax problem is a classic shock tube problem, the initial condition is taken as [44]

$$(\rho, u, p) = \begin{cases} (0.445, 0.698, 3.528), & x \in [-0.5, 0), \\ (0.5, 0, 0.571), & x \in [0, 0.5]. \end{cases} \tag{4.2}$$

The computational domain is $[-0.5, 0.5]$ and the final time is $t = 0.16$ in the simulation. Numerical results are given in Figs. 4.1 and 4.2 with grid points $N_x = 100$ and 200. It shows that these indicators can accurately identify the troubled stencil. The results of hybrid schemes are closer to the reference solution than the original WENO method due to its low dissipation. Table 4.1 shows the percentage of troubled stencils and the time ratio of the WENO-H-MLP and WENO-H-SMLP schemes in the entire calculation process. As it can be seen, there is no observable difference between the MLP and SMLP detectors, but the latter is significantly faster.

Table 4.1
Percentage of non-smooth and high-frequency stencil, and time ratio of the Lax problem in Example 4.1.

	WENOJS-H-MLP				WENOJS-H-SMLP				
N_x	Ns	Hf	Ts	RI	Ns	Hf	Ts	RI	RT
100	5.34	2.38	7.72		5.34	2.38	7.72		12.19
200	2.66	1.39	4.05	0.52	2.66	1.39	4.05	0.52	10.71
400	1.31	0.79	2.10	0.52	1.31	0.79	2.10	0.52	9.71
800	0.63	0.45	1.08	0.52	0.63	0.45	1.08	0.52	9.53
	WENOZ-H-MLP				WENOZ-H-SMLP				
N_x	Ns	Hf	Ts	RI	Ns	Hf	Ts	RI	RT
100	5.35	2.37	7.72		5.35	2.37	7.72		9.95
200	2.66	1.38	4.04	0.52	2.66	1.38	4.04	0.52	9.68
400	1.31	0.78	2.09	0.52	1.31	0.78	2.09	0.52	9.20
800	0.64	0.44	1.08	0.52	0.64	0.44	1.08	0.52	8.72

Example 4.2 (*The Sod Problem*). Sod problem is another shock tube problem, the initial condition is taken as [7]

$$(\rho, u, p) = \begin{cases} (1, 0, 1), & x \in [-5, 0), \\ (0.125, 0, 0.1), & x \in [0, 5]. \end{cases} \tag{4.3}$$

The computational domain is $[-5, 5]$ and the final time is $t = 2$. The reference solution is given by the fifth-order finite difference WENOJS scheme with 1600 grid points. Fig. 4.3 shows the solution by hybridization of two detectors almost overlaps in each subfigure with grid points $N_x = 100$ and 200 and maintains the characteristic of essentially oscillation-free. However, the MLP and SMLP detectors indicate a little differently when $N_x = 200$ in Fig. 4.4, the indication results are almost the same with the refinement of grids. Meanwhile, the SMLP detector is much more efficient where $RT \approx 8$ (see Table 4.2).

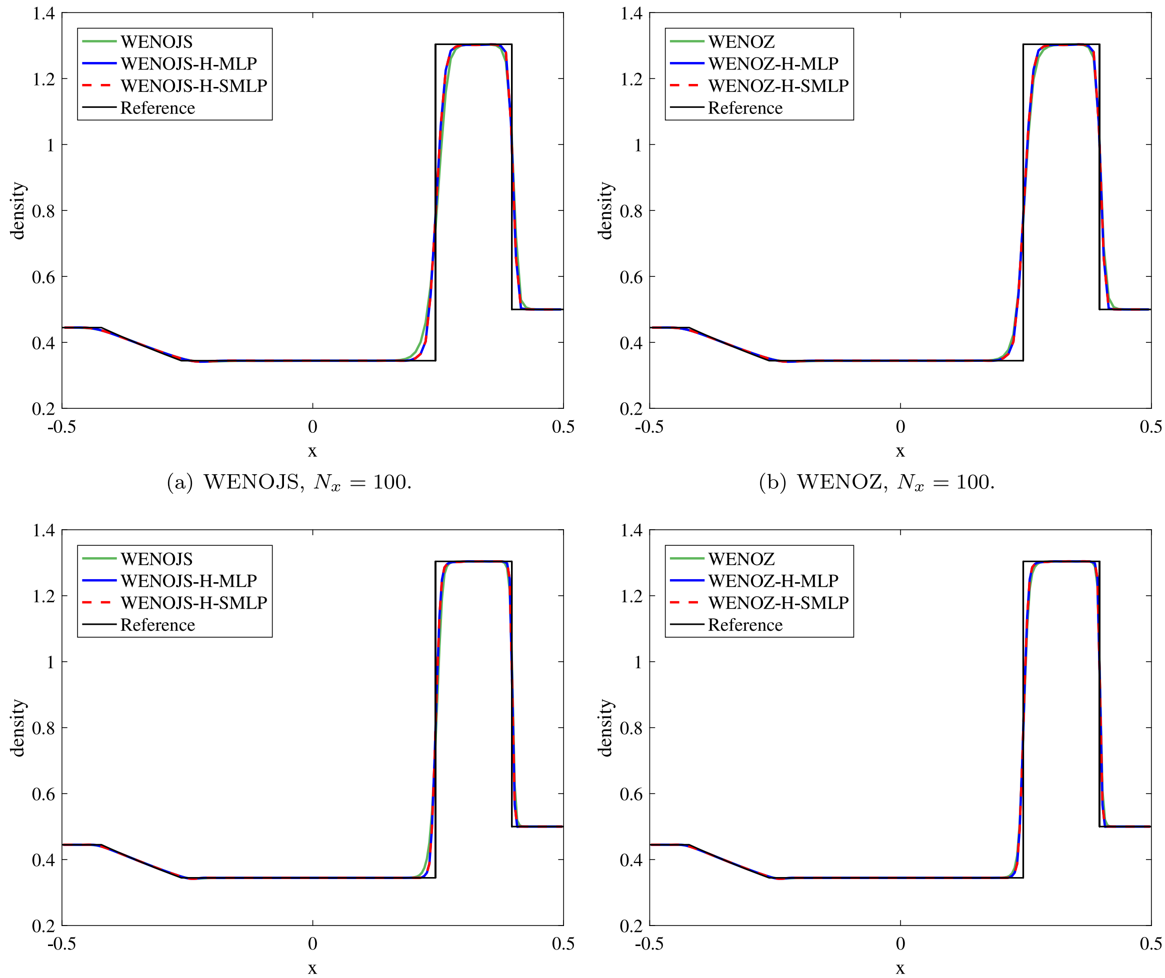

(a) WENOJS, $N_x = 100$.
(b) WENOZ, $N_x = 100$.
(c) WENOJS, $N_x = 200$.
(d) WENOZ, $N_x = 200$.

Fig. 4.1. Numerical results for the Lax problem in Example 4.1. First column: $N_x = 100$. Second column: $N_x = 200$.

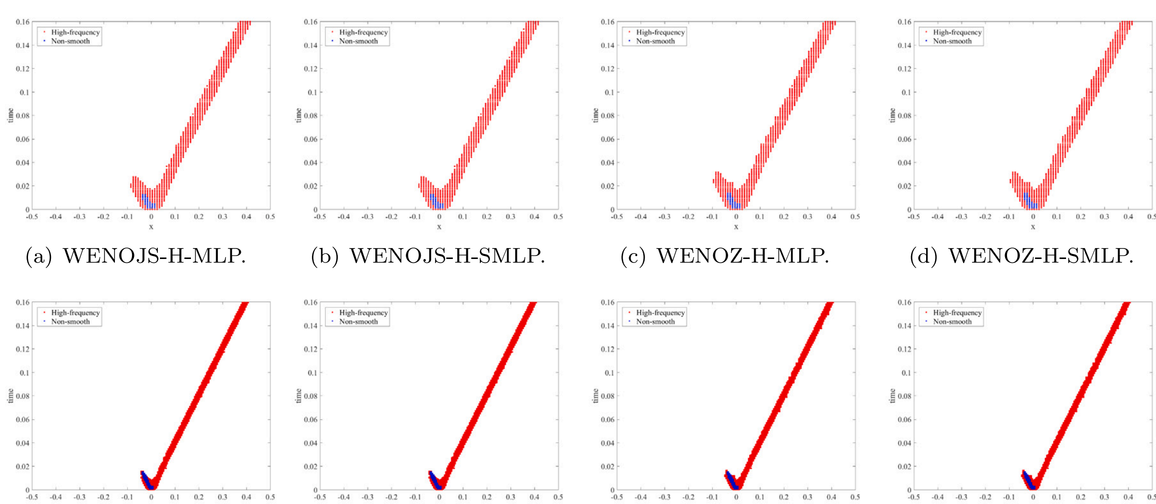

(a) WENOJS-H-MLP.
(b) WENOJS-H-SMLP.
(c) WENOZ-H-MLP.
(d) WENOZ-H-SMLP.
(e) WENOJS-H-MLP.
(f) WENOJS-H-SMLP.
(g) WENOZ-H-MLP.
(h) WENOZ-H-SMLP.

Fig. 4.2. Non-smooth and high-frequency stencils of different schemes for the Lax problem in Example 4.1, First row: $N_x = 100$. Second row: $N_x = 200$. First column: WENOJS-H-MLP. Second column: WENOJS-H-SMLP. Third column: WENOZ-H-MLP. Fourth column: WENOZ-H-SMLP.

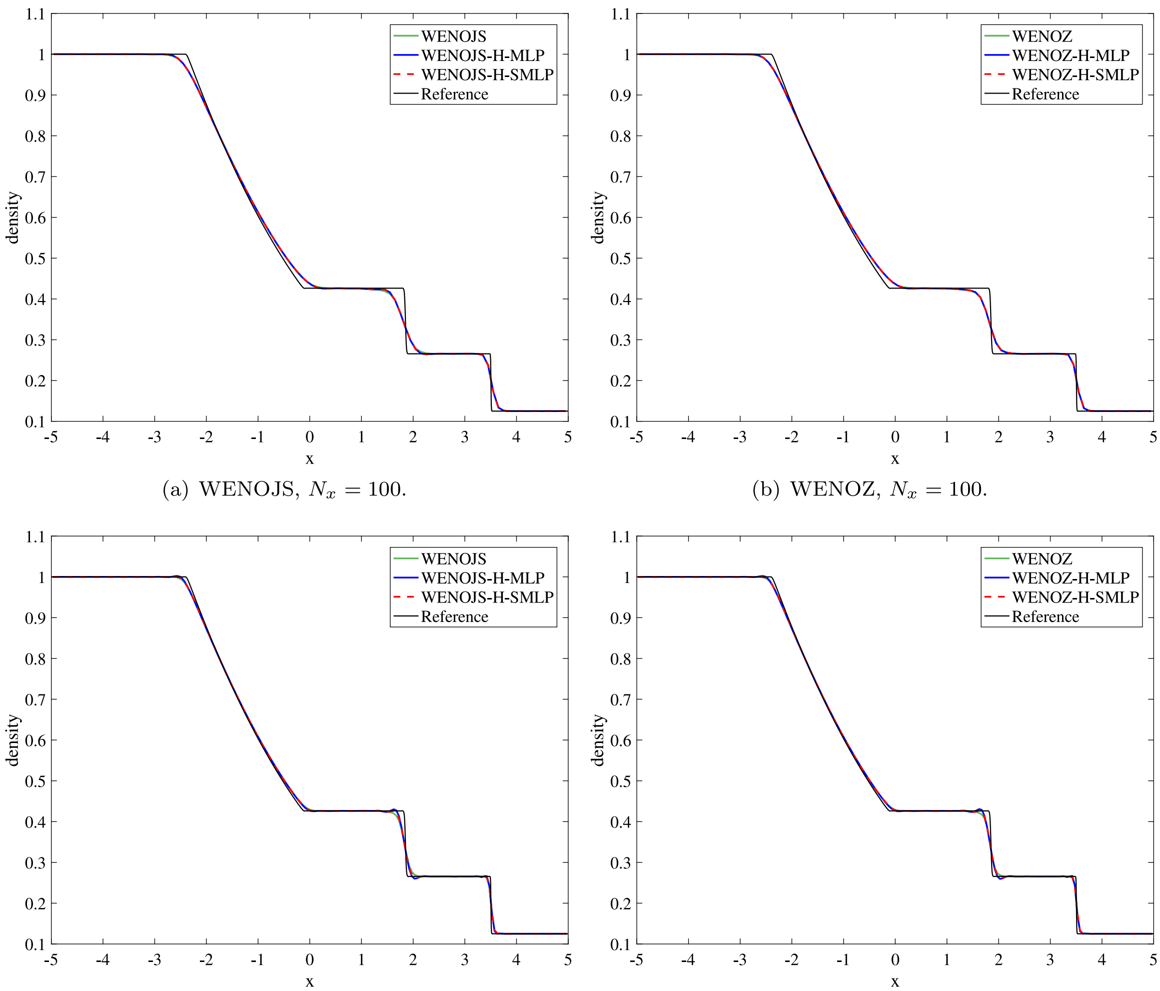

(a) WENOJS, $N_x = 100$. (b) WENOZ, $N_x = 100$.

(c) WENOJS, $N_x = 200$. (d) WENOZ, $N_x = 200$.

Fig. 4.3. Numerical results for the Sod problem in Example 4.2. First column: $N_x = 100$. Second column: $N_x = 200$.

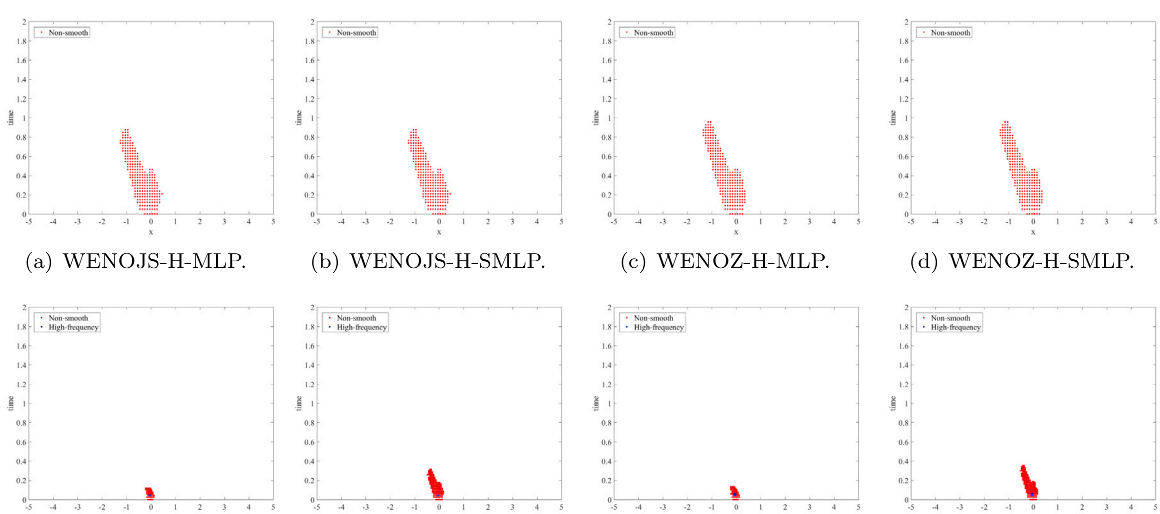

(a) WENOJS-H-MLP. (b) WENOJS-H-SMLP. (c) WENOZ-H-MLP. (d) WENOZ-H-SMLP.

(e) WENOJS-H-MLP. (f) WENOJS-H-SMLP. (g) WENOZ-H-MLP. (h) WENOZ-H-SMLP.

Fig. 4.4. Non-smooth and high-frequency stencil of different schemes for the Sod problem in Example 4.2, First row: $N_x = 100$. Second row: $N_x = 200$. First column: WENOJS-H-MLP. Second column: WENOJS-H-SMLP. Third column: WENOZ-H-MLP. Fourth column: WENOZ-H-SMLP.

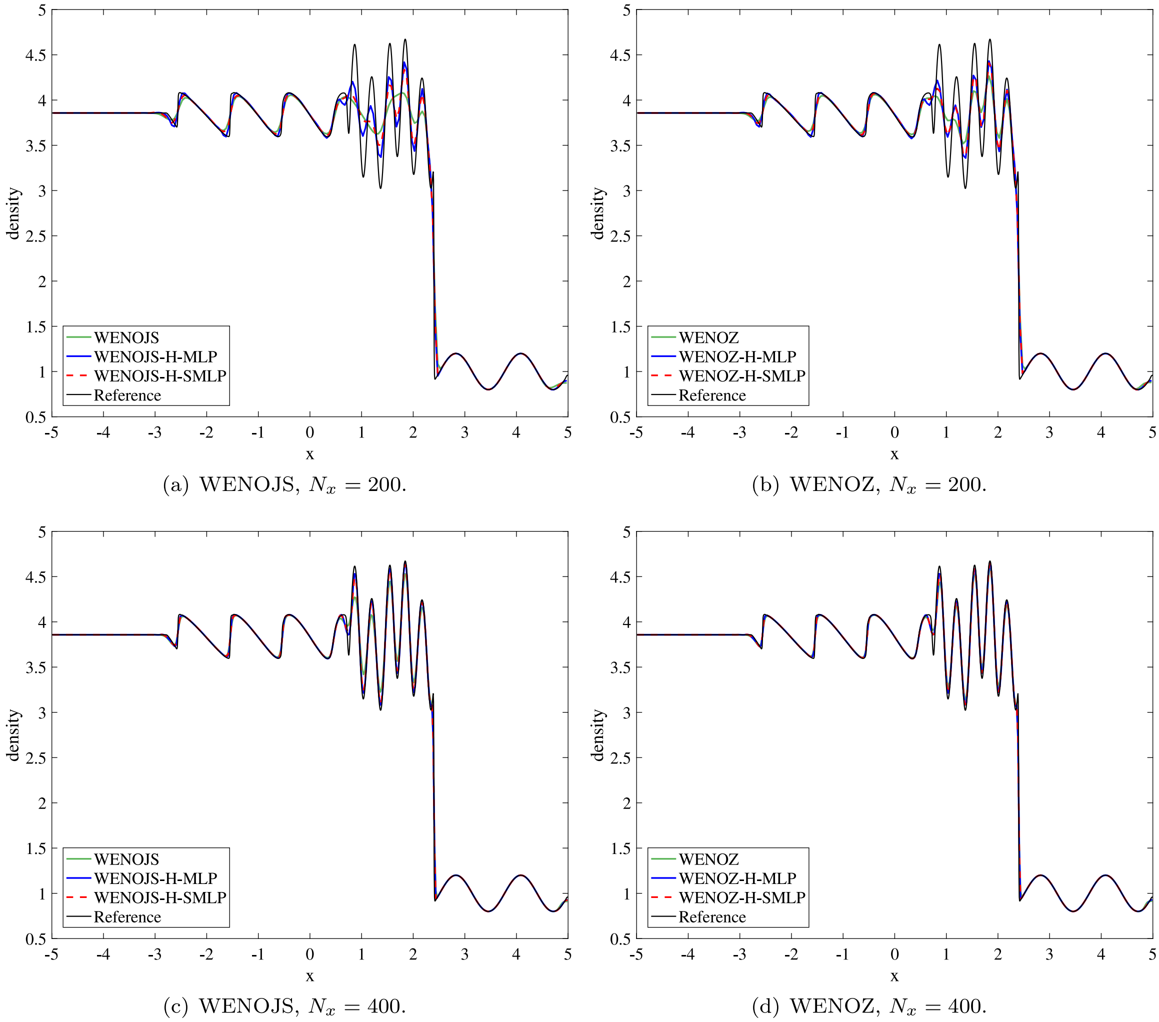

(a) WENOJS, $N_x = 200$. (b) WENOZ, $N_x = 200$.

(c) WENOJS, $N_x = 400$. (d) WENOZ, $N_x = 400$.

Fig. 4.5. Numerical results for the Shu–Osher problem in Example 4.3. First column: $N_x = 200$. Second column: $N_x = 400$.

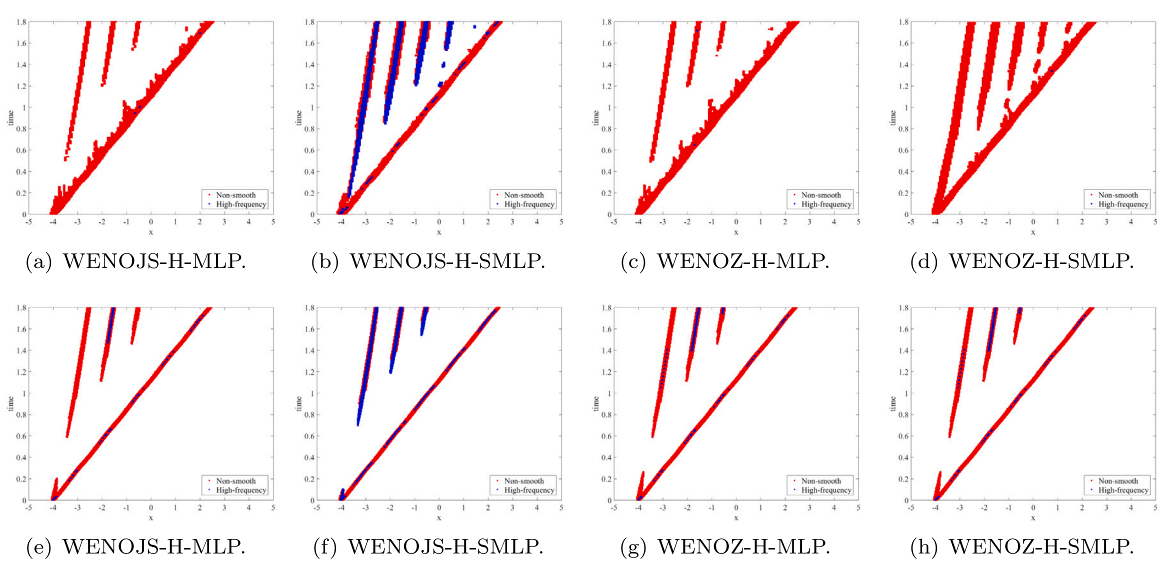

(a) WENOJS-H-MLP. (b) WENOJS-H-SMLP. (c) WENOZ-H-MLP. (d) WENOZ-H-SMLP.

(e) WENOJS-H-MLP. (f) WENOJS-H-SMLP. (g) WENOZ-H-MLP. (h) WENOZ-H-SMLP.

Fig. 4.6. Non-smooth and high-frequency stencil of different schemes for the Shu–Osher problem in Example 4.3, First row: $N_x = 200$. Second row: $N_x = 400$. First column: WENOJS-H-MLP. Second column: WENOJS-H-SMLP. Third column: WENOZ-H-MLP. Fourth column: WENOZ-H-SMLP.

Table 4.2
Percentage of non-smooth and high-frequency stencil, and time ratio of the Sod problem in Example 4.2.

	WENOJS-H-MLP				WENOJS-H-SMLP				
N_x	Ns	Hf	Ts	RI	Ns	Hf	Ts	RI	RT
100	3.59	0	3.59		3.59	0	3.59		7.99
200	0.54	0	0.54	0.15	1.01	0	1.01	0.28	9.53
400	0.49	0.01	0.50	0.93	0.49	0.01	0.50	0.50	8.03
800	0.22	0.02	0.24	0.48	0.22	0.02	0.24	0.48	8.00
	WENOZ-H-MLP				WENOZ-H-SMLP				
N_x	Ns	Hf	Ts	RI	Ns	Hf	Ts	RI	RT
100	4.28	0	4.28		4.28	0	4.28		8.21
200	0.54	0.01	0.55	0.13	1.09	0	1.09	0.25	8.19
400	0.52	0.01	0.53	0.97	0.52	0.01	0.53	0.49	8.24
800	0.23	0.02	0.25	0.47	0.23	0.02	0.25	0.47	8.11

Table 4.3
Percentage of non-smooth and high-frequency stencil, and time ratio of the Shu–Osher problem in Example 4.3.

	WENOJS-H-MLP				WENOJS-H-SMLP				
N_x	Ns	Hf	Ts	RI	Ns	Hf	Ts	RI	RT
100	29.37	1.03	30.40		29.37	1.08	30.45		10.45
200	2.53	1.71	4.24	0.14	4.53	1.71	6.24	0.21	9.40
400	1.61	1.59	3.20	0.75	1.61	1.59	3.20	0.51	8.89
800	0.7	0.32	1.02	0.32	0.70	0.32	1.02	0.32	8.18
	WENOZ-H-MLP				WENOZ-H-SMLP				
N_x	Ns	Hf	Ts	RI	Ns	Hf	Ts	RI	RT
100	29.47	1.04	30.51		29.48	1.10	30.57		10.26
200	2.63	1.73	4.35	0.14	4.67	1.78	6.46	0.21	9.81
400	1.66	1.59	3.25	0.75	1.66	1.59	3.25	0.50	8.87
800	0.71	0.32	1.04	0.32	0.71	0.32	1.04	0.32	8.25

Example 4.3 (*The Shu–Osher Problem*)**.** The Shu–Osher problem [7] is considered here whose initial condition is

$$(\rho, u, p) = \begin{cases} (3.857143, 2.629369, 10.333333), & x \in [-5, -4), \\ (1 + 0.2\sin(5x), 0, 0.1), & x \in [-4, 5]. \end{cases} \tag{4.4}$$

It describes that a Mach 3 shock wave interacts with a density disturbance that generates a flow field with smooth structures and discontinuities. The density of the numerical results at $t = 1.8$ with grid points $N_x = 200$ and 400 are shown in Fig. 4.5. The reference solution is given by the fifth-order finite difference WENOJS scheme with 1600 grid points. When the grid points $N_x = 200$, the WENOJS and WENOZ methods cannot obtain accurate wave numbers near the high-wavenumber region because of numerical dissipation, but the hybrid schemes can. When the grid is refined to $N_x = 400$, the hybrid schemes are closer to the reference solution than the original schemes. From Fig. 4.6 and Table 4.3, there is a bit difference between the two detectors when the grid points are equal to 200 because the structure of the solution is complex. But after the grid points are refined, the indication results of the two detectors are almost the same. And the efficiency of the SMLP detector is about ten times faster than the MLP detector.

Example 4.4 (*The Blast Wave Problem*)**.** This problem was first proposed by Woodward and Colella [45]. It depicts the interaction of two blast waves. The initial condition is given by

$$(\rho, u, p) = \begin{cases} (1, 0, 1), & x \in (0, 0.1), \\ (1, 0, 0.01), & x \in (0.1, 0.9), \\ (1, 0, 100), & x \in (0.9, 1). \end{cases} \tag{4.5}$$

Table 4.4
Percentage of non-smooth and high-frequency stencils, and time ratio of the blast wave problem in Example 4.4.

	WENOJS-H-MLP				WENOJS-H-SMLP				
N_x	Ns	Hf	Ts	RI	Ns	Hf	Ts	RI	RT
100	5.09	21.37	26.46		5.09	21.37	26.46		11.63
200	2.20	11.21	13.41	0.51	2.20	11.21	13.41	0.51	9.58
400	0.90	5.82	6.72	0.50	0.90	5.82	6.72	0.50	9.27
800	0.38	3.21	3.59	0.53	0.38	3.21	3.59	0.53	8.67
	WENOZ-H-MLP				WENOZ-H-SMLP				
N_x	Ns	Hf	Ts	RI	Ns	Hf	Ts	RI	RT
100	5.21	21.09	26.31		5.21	21.1	26.31		10.44
200	2.29	11.04	13.33	0.51	2.30	11.04	13.34	0.51	9.30
400	0.96	5.72	6.68	0.50	0.96	5.72	6.68	0.50	8.68
800	0.40	3.16	3.57	0.53	0.40	3.16	3.57	0.53	8.52

Table 4.5
Percentage of non-smooth and high-frequency stencil, and time ratio of the Riemann problem 1 in Example 4.5.

	WENOJS-H-MLP				WENOJS-H-SMLP				
$N_x \times N_y$	Ns	Hf	Ts	RI	Ns	Hf	Ts	RI	RT
100 × 100	5.83	0.93	6.76		5.83	0.93	6.76		23.40
200 × 200	2.89	0.63	3.52	0.52	2.89	0.63	3.52	0.52	20.76
400 × 400	1.42	0.42	1.83	0.52	1.42	0.42	1.83	0.52	16.08
800 × 800	0.68	0.26	0.94	0.51	0.68	0.26	0.94	0.51	14.88
	WENOZ-H-MLP				WENOZ-H-SMLP				
$N_x \times N_y$	Ns	Hf	Ts	RI	Ns	Hf	Ts	RI	RT
100 × 100	6.08	0.97	7.06		6.09	0.97	7.06		21.36
200 × 200	3.02	0.66	3.68	0.52	3.02	0.66	3.68	0.52	20.68
400 × 400	1.46	0.43	1.89	0.51	1.46	0.43	1.89	0.51	15.90
800 × 800	0.69	0.27	0.96	0.51	0.69	0.27	0.96	0.51	14.69

Reflection boundaries are used at $x = 0$ and $x = 1$, and the final time is $t = 0.038$. The reference solution is given by the fifth-order finite difference WENOJS method with 1600 grid points. From the numerical solution in Fig. 4.7 and the marked stencils in Fig. 4.8, it can be seen that the indication results and numerical solutions of the two detectors are very similar. Table 4.4 also verifies this observation. At the same time, in this test, these detectors accurately distinguish the structure of the solution, where the ratios RI are all close to 0.5. And $RT = 8 \sim 10$ shows the efficiency of the SMLP detector.

Example 4.5 (*Riemann Problem 1*)**.** This is a classic Riemann problem [46], with the initial condition

$$(\rho, u, v, p) = \begin{cases} (1.5, 0, 0, 1.5), & x > 0.8, y > 0.8, \\ (0.5323, 1.206, 0, 0), & x < 0.8, y > 0.8, \\ (0.138, 1.206, 1.206, 0.029), & x < 0.8, y < 0.8, \\ (0.5323, 0, 1.206, 0, 0.3), & x > 0.8, y < 0.8. \end{cases} \tag{4.6}$$

The computational domain is $[0, 1] \times [0, 1]$, and the final time is $t = 0.8$. Four sets of grids $N_x \times N_y = 100 \times 100$, 200×200, 400×400 and 800×800 are used. The density of the numerical results on 400×400 are shown in Fig. 4.9. Small vortices near the slip lines are observed by both hybrid schemes WENO-H-MLP and WENO-H-SMLP, while they are damped by the WENOJS method. In addition, the numerical solutions of WENO-H-MLP and WENO-H-SMLP schemes also have more obvious vortices than the WENOZ method due to their better spectral property. The troubled stencil is well indicated by both detectors, as shown in Fig. 4.10. Table 4.5 shows the efficiency of the SMLP detector with $RT \approx 15$.

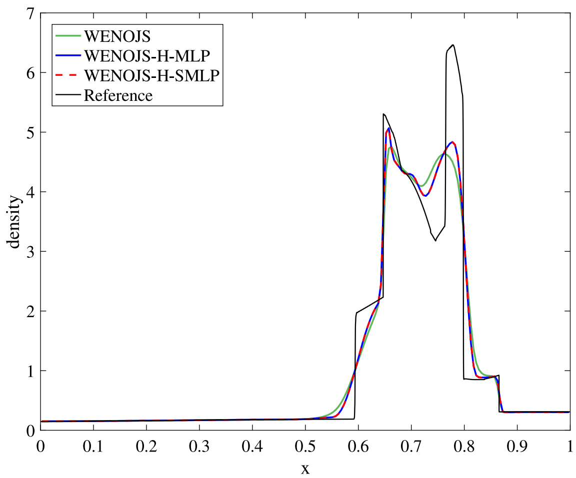

(a) WENOJS, $N_x = 200$.

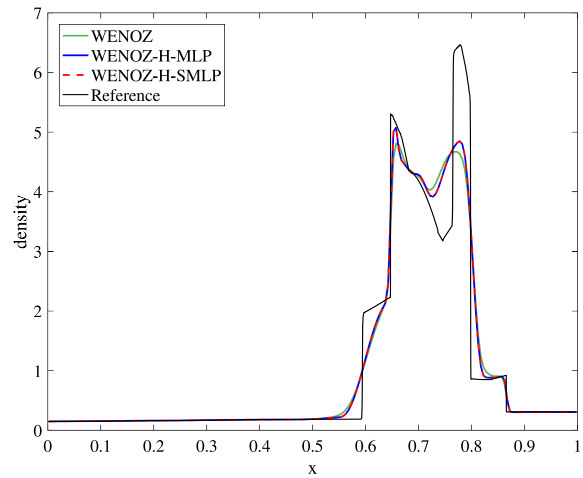

(b) WENOZ, $N_x = 200$.

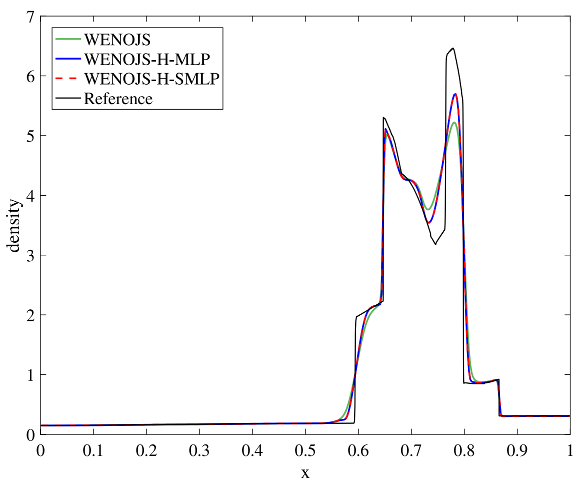

(c) WENOJS, $N_x = 400$.

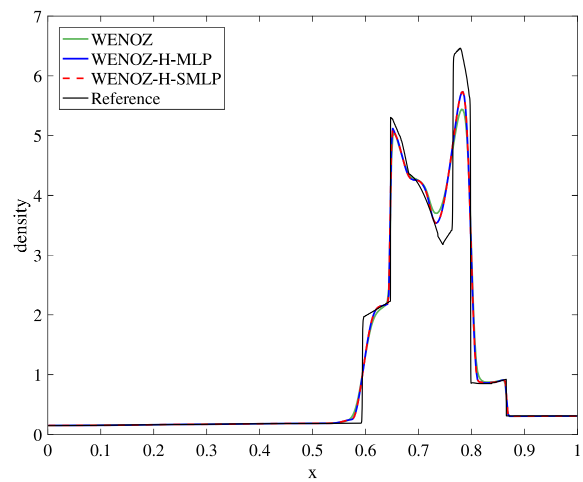

(d) WENOZ, $N_x = 400$.

Fig. 4.7. Numerical results for the blast wave problem in Example 4.4. First column: $N_x = 200$. Second column: $N_x = 400$.

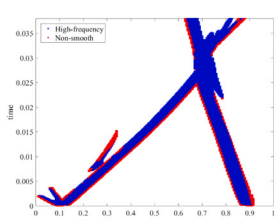

(a) WENOJS-H-MLP.

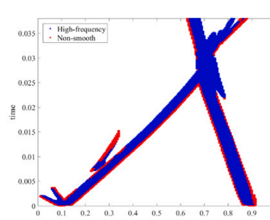

(b) WENOJS-H-SMLP.

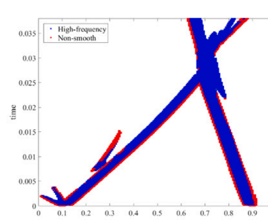

(c) WENOZ-H-MLP.

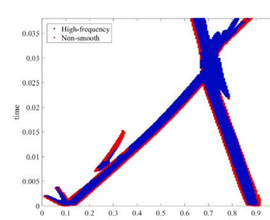

(d) WENOZ-H-SMLP.

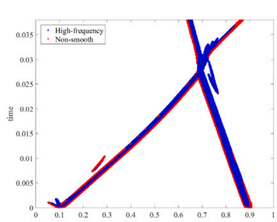

(e) WENOJS-H-MLP.

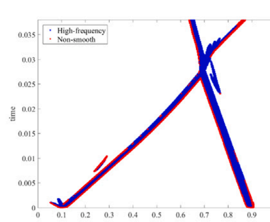

(f) WENOJS-H-SMLP.

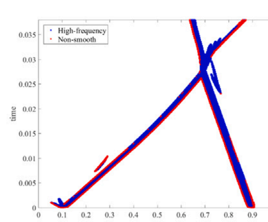

(g) WENOZ-H-MLP.

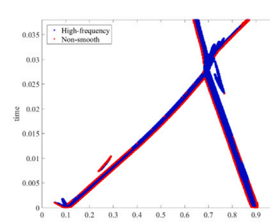

(h) WENOZ-H-SMLP.

Fig. 4.8. Non-smooth and high-frequency stencil of different schemes for the blast wave problem in Example 4.4. First row: $N_x = 200$. Second row: $N_x = 400$. First column: WENOJS-H-MLP. Second column: WENOJS-H-SMLP. Third column: WENOZ-H-MLP. Fourth column: WENOZ-H-SMLP.

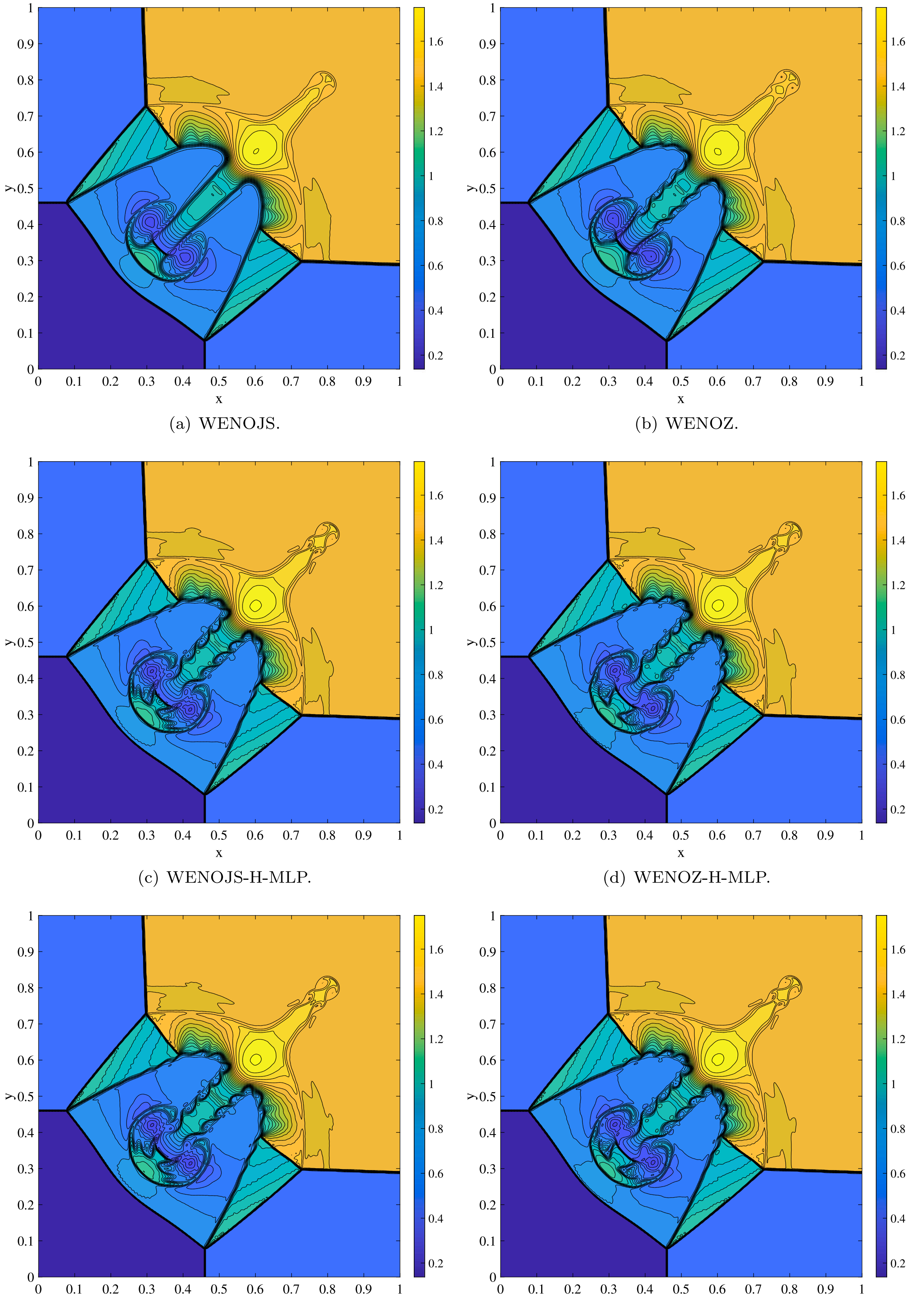

(a) WENOJS. (b) WENOZ.

(c) WENOJS-H-MLP. (d) WENOZ-H-MLP.

(e) WENOJS-H-SMLP. (f) WENOZ-H-SMLP.

Fig. 4.9. Numerical results for the Riemann problem 1 in Example 4.5. $N_x \times N_y = 400 \times 400$ at $t = 0.8$, 35 equally spaced density contours from 0.1 to 1.8.

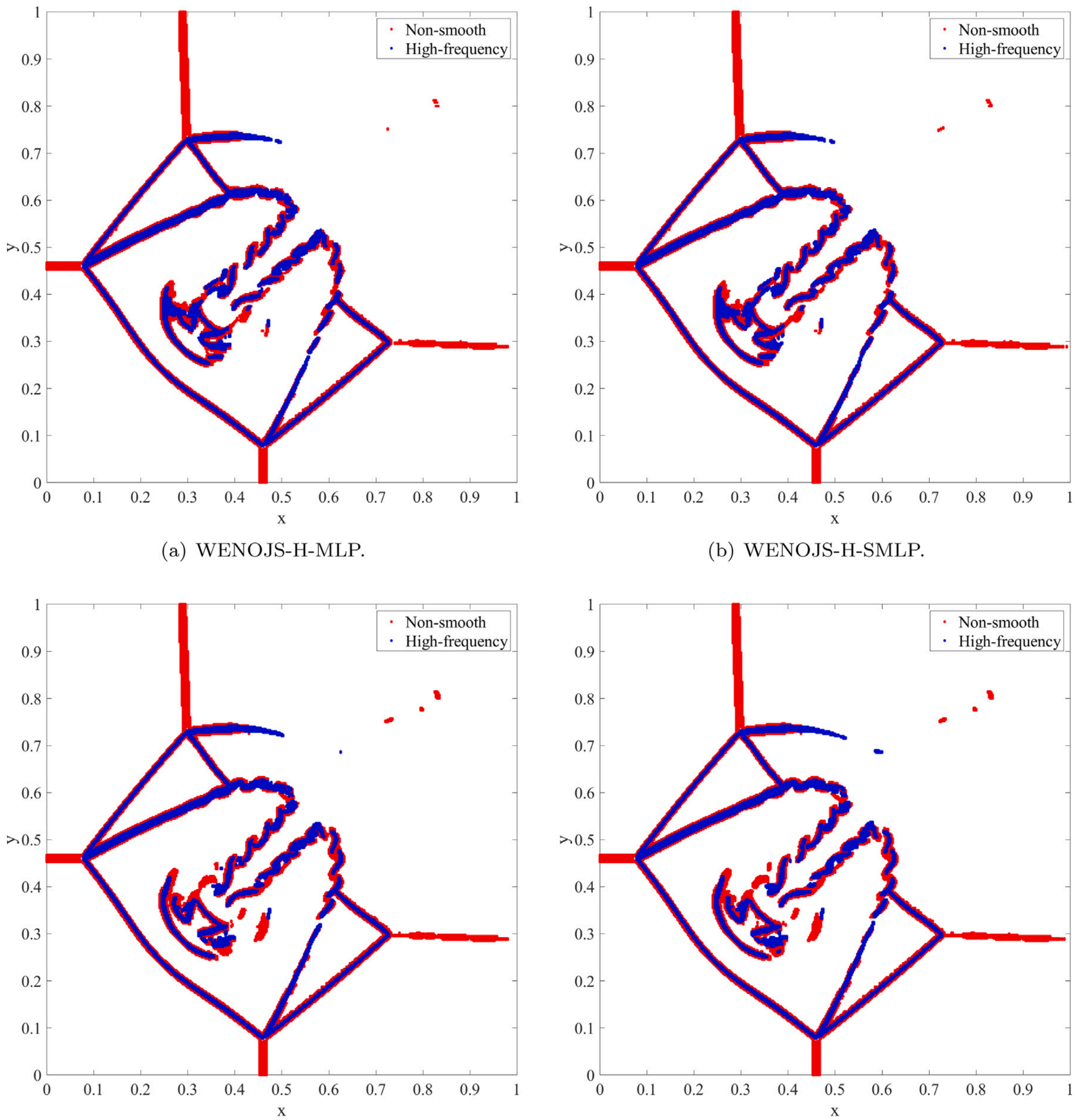

(a) WENOJS-H-MLP.

(b) WENOJS-H-SMLP.

(c) WENOZ-H-MLP.

(d) WENOZ-H-SMLP.

Fig. 4.10. Non-smooth s and high-frequency stencil of different schemes for the Riemann problem 1 in Example 4.5 on $N_x \times N_y = 400 \times 400$ at $t = 0.8$.

Example 4.6 (*Riemann Problem 2*)**.** This is another Riemann problem [46], the initial condition is taken as

$$(\rho, u, v, p) = \begin{cases} (1, 0.75, -0.5, 1), & x > 0.5, y > 0.5, \\ (2, 0.75, 0.5, 1), & x < 0.5, y > 0.5, \\ (1, -0.75, 0.5, 1), & x < 0.5, y < 0.5, \\ (3, -0.75, -0.5, 1), & x > 0.5, y < 0.5. \end{cases} \tag{4.7}$$

The computational domain is $[0, 1] \times [0, 1]$, and the final time is $t = 0.3$. Four sets of grids $N_x \times N_y = 200 \times 200$, 400×400, 800×800 and 1600×1600 are used. The density of the numerical results on grid points 1600×1600 and the corresponding marked stencils are shown in Figs. 4.11 and 4.12. Compared with the original WENO method, the hybrid schemes observe many small vortices structures near the four slip lines. It is observed from Table 4.6 that the value of RI increases a little bit with the refinement of mesh, but it is still around 0.5 since more structures on the slip line are displayed. Besides, the SMLP detector is at least 15 times faster than the MLP detector.

Table 4.6
Percentage of non-smooth and high-frequency stencil, and time ratio of the Riemann problem 2 in Example 4.6.

	WENOJS-H-MLP				WENOJS-H-SMLP				
$N_x \times N_y$	Ns	Hf	Ts	RI	Ns	Hf	Ts	RI	RT
200 × 200	1.43	0.45	1.88		1.43	0.45	1.88		20.34
400 × 400	0.59	0.28	0.87	0.46	0.59	0.28	0.87	0.46	18.32
800 × 800	0.24	0.17	0.41	0.47	0.24	0.17	0.41	0.47	15.61
1600 × 1600	0.11	0.11	0.21	0.52	0.11	0.11	0.21	0.52	17.61
	WENOZ-H-MLP				WENOZ-H-SMLP				
$N_x \times N_y$	Ns	Hf	Ts	RI	Ns	Hf	Ts	RI	RT
200 × 200	1.48	0.45	1.93		1.48	0.45	1.93		20.61
400 × 400	0.61	0.28	0.89	0.46	0.61	0.28	0.89	0.46	16.92
800 × 800	0.24	0.17	0.42	0.47	0.24	0.17	0.42	0.47	15.63
1600 × 1600	0.11	0.11	0.22	0.52	0.11	0.11	0.22	0.52	17.09

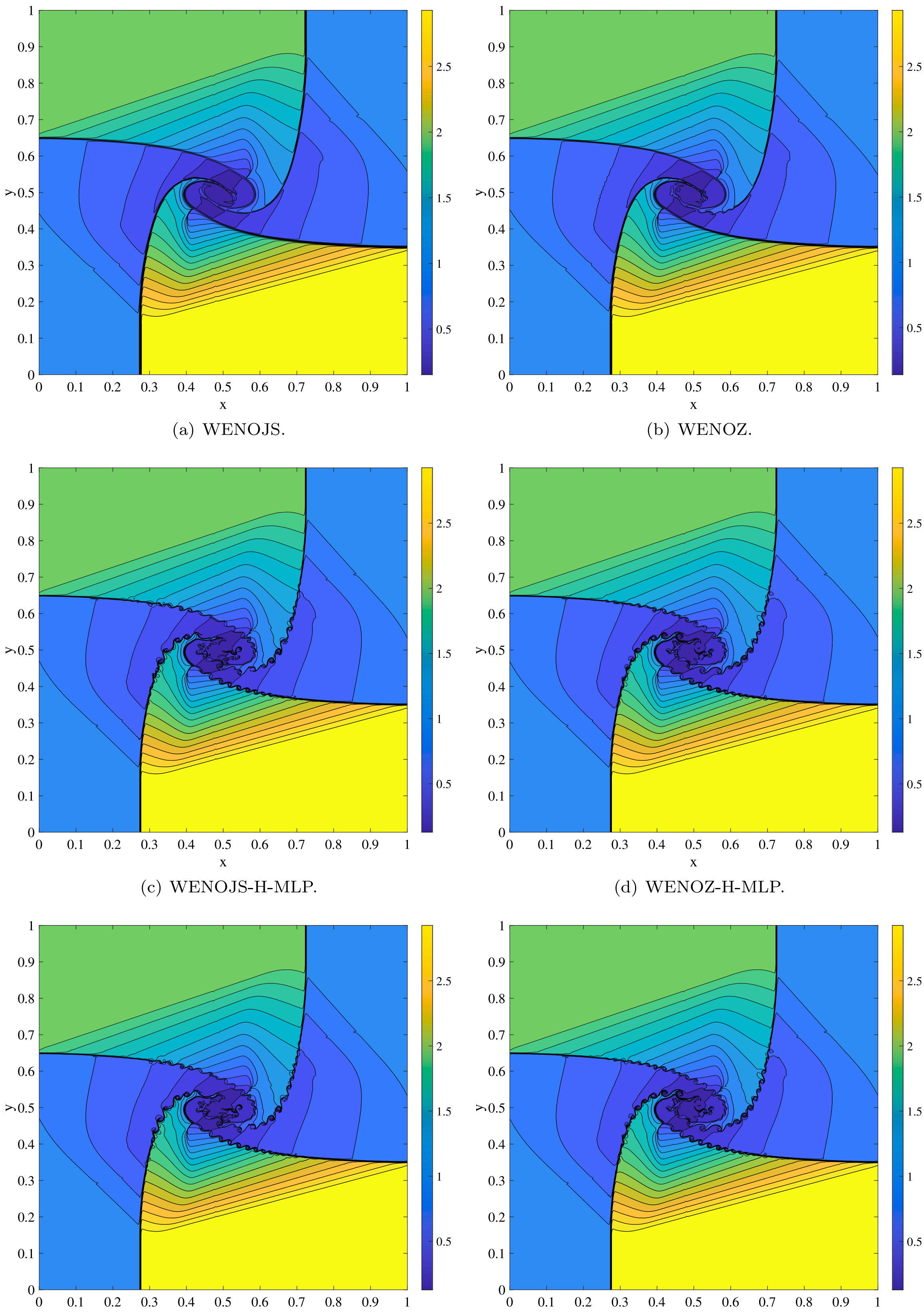

(a) WENOJS.

(b) WENOZ.

(c) WENOJS-H-MLP.

(d) WENOZ-H-MLP.

(e) WENOJS-H-SMLP.

(f) WENOZ-H-SMLP.

Fig. 4.11. Numerical results for the Riemann problem 2 in Example 4.6. $N_x \times N_y = 1600 \times 1600$ at $t = 0.3$, 20 equally spaced density contours.

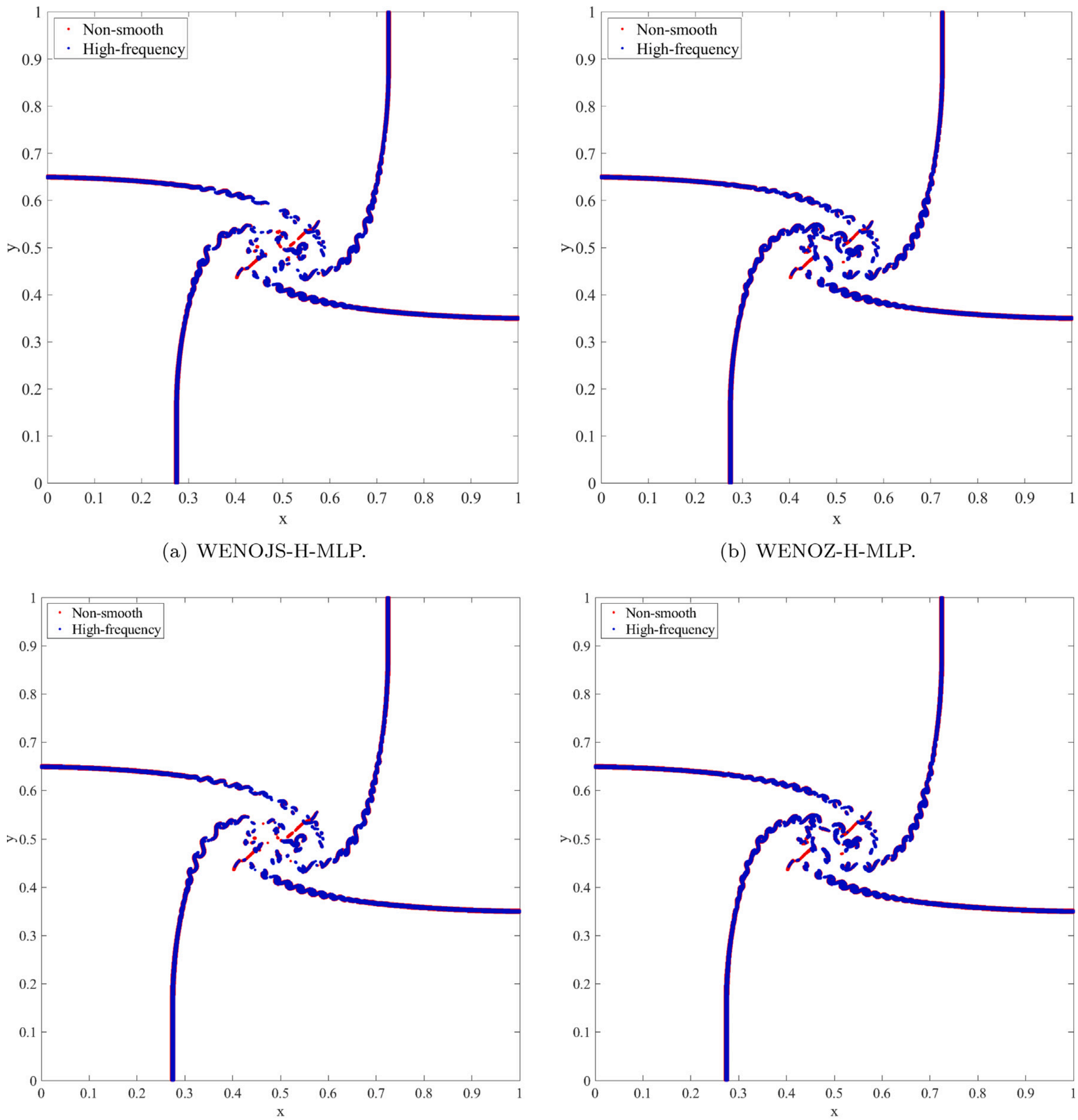

(a) WENOJS-H-MLP. (b) WENOZ-H-MLP.

(c) WENOJS-H-SMLP. (d) WENOZ-H-SMLP.

Fig. 4.12. Non-smooth s and high-frequency stencil of different schemes for the Riemann problem 2 in Example 4.6 on $N_x \times N_y = 1600 \times 1600$ at $t = 0.3$.

Example 4.7 (*Double Mach Reflection*)**.** This problem was introduced by Woodward and Colella [45]. It describes a shock with a velocity of Mach 10 hitting a reflective wall at an angle of 60°. The density of the air in front of the shock is 1.4, and the pressure is 1. The computational domain is $[0,4] \times [0,1]$ and the final time is $t = 0.2$. The reflecting wall is at the bottom of the problem domain from $x = \frac{1}{6}$ to $x = 4$, reflective boundary conditions are used in this region. Post-shock condition is used in the bottom of the problem domain from $x = 0$ to $x = \frac{1}{6}$. The exact boundary conditions to describe the motion of the shock wave are used at the top of the problem domain. And inflow and outflow boundary conditions are used for the left and right boundaries respectively. The initial condition is

$$(\rho, u, v, p) = \begin{cases} (1.4, 0.0, 0.0, 1.0), & y < \sqrt{3}\left(x - \frac{1}{6}\right), \\ (8.0, 7.145, -4.125, 116.5), & y \geq \sqrt{3}\left(x - \frac{1}{6}\right). \end{cases} \tag{4.8}$$

Four sets of grids $N_x \times N_y = 120 \times 30, 240 \times 60, 480 \times 120$ and 960×240 are chosen respectively. The density of the numerical results on grid points 960×240, and the corresponding marked stencils are shown in Figs. 4.13 and 4.14. As shown in Fig. 4.13, the more small vortex structures are observed near the slip line, and the wall jet by the hybrid schemes WENO-H-MLP and WENO-H-SMLP compared to original schemes WENOJS and WENOZ. Both the MLP and SMLP indicators can accurately identify the troubled stencil by shock waves and contact discontinuities from Fig. 4.13. In Table 4.7, it shows that the SMLP detector significantly reduce the cost of the MLP detector, where $RT = 15 \sim 22$.

5. Conclusion

This paper first designed an MLP smoothness detector based on error metrics for the hybrid WENO scheme. And then, it has been simplified to an SMLP detector, which can significantly reduce the cost of the original one. Both detectors have been integrated into the hybrid WENO schemes with the high-frequency region [33], which shows better spectral approximation property from ADR analysis than

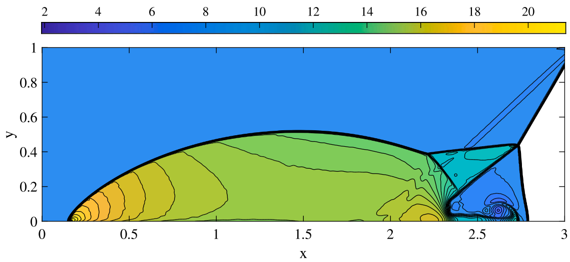

(a) WENOJS.

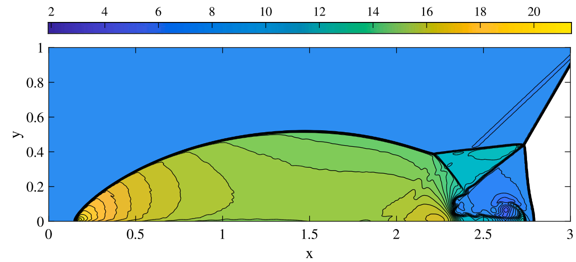

(b) WENOZ.

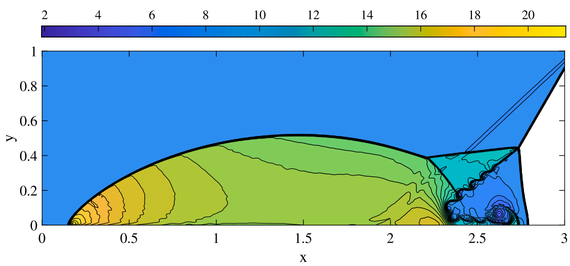

(c) WENOJS-H-MLP.

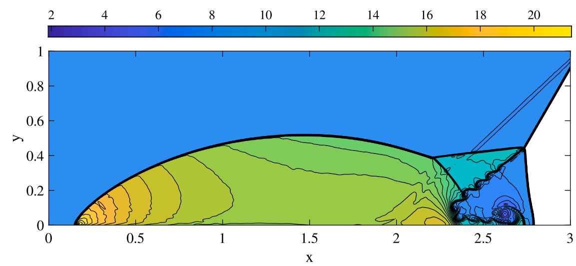

(d) WENOZ-H-MLP.

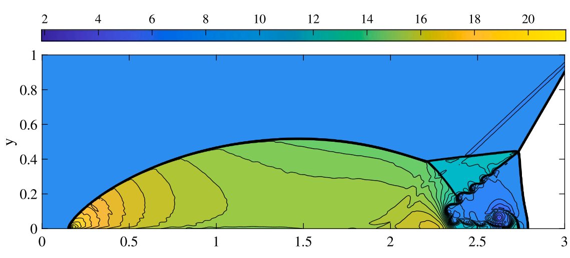

(e) WENOJS-H-SMLP.

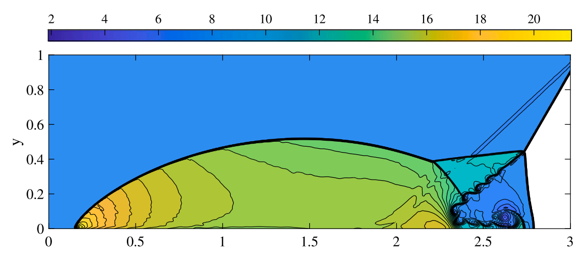

(f) WENOZ-H-SMLP.

Fig. 4.13. Numerical results for the double Mach reflection in Example 4.7. $N_x \times N_y = 960 \times 240$ at $t = 0.3$, 43 equally spaced density contours from 1.887 to 22.9.

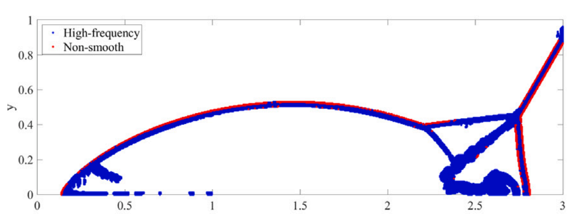

(a) WENOJS-H-MLP.

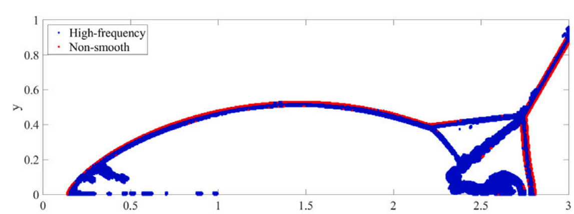

(b) WENOZ-H-MLP.

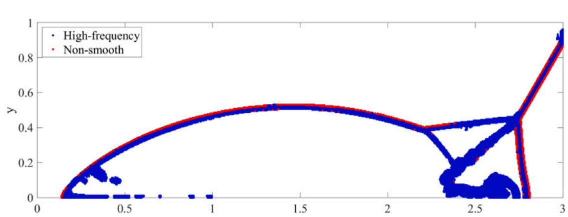

(c) WENOJS-H-SMLP.

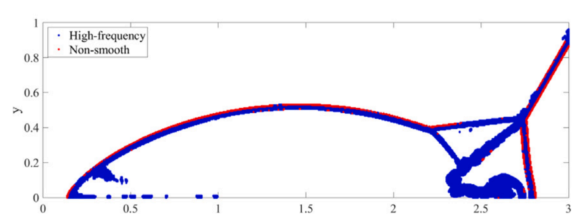

(d) WENOZ-H-SMLP.

Fig. 4.14. Non-smooth and high-frequency stencil of different schemes for the double Mach reflection in Example 4.7 on $N_x \times N_y = 960 \times 240$ at final time $t = 0.3$.

Table 4.7
Percentage of non-smooth and high-frequency stencil, and time ratio of the double Mach reflection in Example 4.7.

	WENOJS-H-MLP				WENOJS-H-SMLP				
$N_x \times N_y$	Ns	Hf	Ts	RI	Ns	Hf	Ts	RI	RT
120 × 30	3.41	9.25	12.66		3.41	9.26	12.67		22.00
240 × 60	1.62	5.25	6.88	0.54	1.62	5.25	6.88	0.54	18.62
480 × 120	0.76	2.84	3.60	0.52	0.76	2.85	3.61	0.52	15.81
960 × 240	0.34	1.51	1.85	0.51	0.34	1.51	1.85	0.51	15.20
	WENOZ-H-MLP				WENOZ-H-SMLP				
$N_x \times N_y$	Ns	Hf	Ts	RI	Ns	Hf	Ts	RI	RT
120 × 30	3.42	9.24	12.66		3.42	9.24	12.66		22.00
240 × 60	1.62	5.24	6.86	0.54	1.62	5.24	6.86	0.54	17.36
480 × 120	0.76	2.83	3.59	0.52	0.76	2.83	3.59	0.52	16.15
960 × 240	0.34	1.51	1.85	0.51	0.34	1.50	1.84	0.51	15.01

the original WENO schemes. These schemes have been applied to Euler equations in one and two dimensions in the numerical tests. From the comparisons with the hybrid/non-hybridized schemes, it has been shown that the hybrid schemes have better resolution and fine-structure capturing property due to their better spectral resolution. Meanwhile, the results of the SMLP detector can maintain the sharp resolution of the MLP detector but are much more efficient.

Declaration of competing interest

The authors declare that they have no known competing financial interests or personal relationships that could have appeared to influence the work reported in this paper.

Funding

The work of Z. Xue was partially supported by the National Numerical Windtunnel Project NNW2019ZT4-B08. The work of Y. Xia was partially supported by the National Numerical Windtunnel Project NNW2019ZT4-B08 and the NSFC grant No. 11871449. The work of C. Li and X. Yuan was partially supported by the National Numerical Windtunnel project, the National Key Research and Development Program of China (2019YFA0405200), and the NSFC grant Nos. 11802324, 92052301.

References

[1] Pirozzoli S. Numerical methods for high-speed flows. Annu Rev Fluid Mech 2011;43:163–94.
[2] Wang ZJ, Fidkowski K, Abgrall R, Bassi F, Caraeni D, Cary A, Deconinck H, Hartmann R, Hillewaert K, Huynh HT, et al. High-order CFD methods: current status and perspective. Internat J Numer Methods Fluids 2013;72(8):811–45.
[3] Baccouch M, Temimi H, Ben-Romdhane M. A discontinuous Galerkin method for systems of stochastic differential equations with applications to population biology, finance, and physics. J Comput Appl Math 2021;388:113297.
[4] Giri P, Qiu J. A high-order runge-kutta discontinuous Galerkin method with a subcell limiter on adaptive unstructured grids for two-dimensional compressible inviscid flows. Internat J Numer Methods Fluids 2019;91(8):367–94.
[5] Jiang Z-H, Yan C, Yu J. Implementation of the transition model for high order discontinuous Galerkin method with hybrid discretization strategy. Comput & Fluids 2021;218:104838.
[6] Liu X-D, Osher S, Chan T. Weighted essentially non-oscillatory schemes. J Comput Phys 1994;115(1):200–12.
[7] Jiang G-S, Shu C-W. Efficient implementation of weighted ENO schemes. J Comput Phys 1996;126(1):202–28.
[8] Henrick AK, Aslam TD, Powers JM. Mapped weighted essentially non-oscillatory schemes: achieving optimal order near critical points. J Comput Phys 2005;207(2):542–67.
[9] Borges R, Carmona M, Costa B, Don WS. An improved weighted essentially non-oscillatory scheme for hyperbolic conservation laws. J Comput Phys 2008;227(6):3191–211.
[10] Martín MP, Taylor EM, Wu M, Weirs VG. A bandwidth-optimized WENO scheme for the effective direct numerical simulation of compressible turbulence. J Comput Phys 2006;220(1):270–89.
[11] Sun D, Guo Q, Li C, Liu P. Assessment of optimized symmetric fourth-order weighted essentially non-oscillatory scheme in direct numerical simulation of compressible turbulence. Comput & Fluids 2020;197:104383.
[12] Hu X, Wang Q, Adams NA. An adaptive central-upwind weighted essentially non-oscillatory scheme. J Comput Phys 2010;229(23):8952–65.
[13] Li C, Sun D, Guo Q, Liu P, Zhang H. A new hybrid WENO scheme on a four-point stencil for Euler equations. J Sci Comput 2021;87(1):1–37.
[14] Fu L, Hu XY, Adams NA. A family of high-order targeted ENO schemes for compressible-fluid simulations. J Comput Phys 2016;305:333–59.
[15] Hamzehloo A, Lusher DJ, Laizet S, Sandham ND. On the performance of WENO/TENO schemes to resolve turbulence in DNS/LES of high-speed compressible flows. Internat J Numer Methods Fluids 2021;93(1):176–96.
[16] Pirozzoli S. Conservative hybrid compact-WENO schemes for shock-turbulence interaction. J Comput Phys 2002;178(1):81–117.
[17] Ren Y-X, Zhang H, et al. A characteristic-wise hybrid compact-WENO scheme for solving hyperbolic conservation laws. J Comput Phys 2003;192(2):365–86.
[18] Ducros F, Ferrand V, Nicoud F, Weber C, Darracq D, Gacherieu C, Poinsot T. Large-eddy simulation of the shock/turbulence interaction. J Comput Phys 1999;152(2):517–49.
[19] Zhao G-Y, Sun M-B, Pirozzoli S. On shock sensors for hybrid compact/WENO schemes. Comput & Fluids 2020;199:104439.
[20] Hill DJ, Pullin DI. Hybrid tuned center-difference-WENO method for large eddy simulations in the presence of strong shocks. J Comput Phys 2004;194(2):435–50.
[21] Liu S, Shen Y, Peng J, Zhang J. Two-step weighting method for constructing fourth-order hybrid central WENO scheme. Comput & Fluids 2020;207:104590.
[22] Li G, Qiu J. Hybrid weighted essentially non-oscillatory schemes with different indicators. J Comput Phys 2010;229(21):8105–29.
[23] Brunton SL, Noack BR, Koumoutsakos P. Machine learning for fluid mechanics. Annu Rev Fluid Mech 2020;52:477–508.
[24] Wen X, Don WS, Gao Z, Hesthaven JS. An edge detector based on artificial neural network with application to hybrid compact-WENO finite difference scheme. J Sci Comput 2020;83:1–21.
[25] Sun Z. Convolution neural network shock detector for numerical solution of conservation laws. Commun Comput Phys 2020;28(5).
[26] Feng Y, Liu T, Wang K. A characteristic-featured shock wave indicator for conservation laws based on training an artificial neuron. J Sci Comput 2020;83(1):1–34.
[27] Feng Y, Liu T. A characteristic-featured shock wave indicator on unstructured grids based on training an artificial neuron. J Comput Phys 2021;110446.
[28] Ray D, Hesthaven JS. An artificial neural network as a troubled-cell indicator. J Comput Phys 2018;367:166–91.
[29] Ray D, Hesthaven JS. Detecting troubled-cells on two-dimensional unstructured grids using a neural network. J Comput Phys 2019;397:108845.
[30] Yu X, Shu C-W. Multi-layer perceptron estimator for the total variation bounded constant in limiters for discontinuous galerkin methods. La Mat 2021;1–32.
[31] Zhu H, Wang H, Gao Z. A new troubled-cell indicator for discontinuous Galerkin methods using K-means clustering. SIAM J Sci Comput 2021;43(4):A3009–31.
[32] Discacciati N, Hesthaven JS, Ray D. Controlling oscillations in high-order discontinuous Galerkin schemes using artificial viscosity tuned by neural networks. J Comput Phys 2020;409:109304.
[33] Wan Y, Xia Y. A new hybrid WENO scheme with the high-frequency region for hyperbolic conservation laws. Commun Appl Math Comput 2021. http://dx.doi.org/10.1007/s42967-021-00153-2, (in press).
[34] Roe PL. Approximate Riemann solvers, parameter vectors, and difference schemes. J Comput Phys 1981;43(2):357–72.
[35] Gottlieb S, Shu C-W, Tadmor E. Strong stability-preserving high-order time discretization methods. SIAM Rev 2001;43(1):89–112.
[36] Shu C-W. High order weighted essentially nonoscillatory schemes for convection dominated problems. SIAM Rev 2009;51(1):82–126.
[37] Nasr GE, Badr E, Joun C. Cross entropy error function in neural networks: Forecasting gasoline demand.. In: FLAIRS conference. 2002, p. 381–4.
[38] Kingma DP, Ba J. Adam: A method for stochastic optimization. 2014, arXiv preprint arXiv:1412.6980.
[39] Pirozzoli S. On the spectral properties of shock-capturing schemes. J Comput Phys 2006;219(2):489–97.
[40] Zhao Z, Zhu J, Chen Y, Qiu J. A new hybrid WENO scheme for hyperbolic conservation laws. Comput & Fluids 2019;179:422–36.

[41] Zhao Z, Zhang Y-T, Qiu J. A modified fifth order finite difference Hermite WENO scheme for hyperbolic conservation laws. J Sci Comput 2020;85(2):1–22.

[42] Luo X, Wu S-P. An improved WENO-Z+ scheme for solving hyperbolic conservation laws. J Comput Phys 2021;445:110608.

[43] Wang Z, Zhu J, Yang Y, Tian L, Zhao N. A class of robust low dissipation nested multi-resolution WENO schemes for solving hyperbolic conservation laws. Adv Appl Math Mech 2021;13(5):1064–95.

[44] Lax PD. Weak solutions of nonlinear hyperbolic equations and their numerical computation. Comm Pure Appl Math 1954;7(1):159–93.

[45] Woodward P, Colella P. The numerical simulation of two-dimensional fluid flow with strong shocks. J Comput Phys 1984;54(1):115–73.

[46] Lax PD, Liu X-D. Solution of two-dimensional Riemann problems of gas dynamics by positive schemes. SIAM J Sci Comput 1998;19(2):319–40.